

## Assessing the Impact of Binary Systems on Microlensing Using SPiSEA and PopSyCLE Population Simulations

NATASHA S. ABRAMS,<sup>1</sup> JESSICA R. LU,<sup>1</sup> CASEY Y. LAM,<sup>1,2</sup> MICHAEL S. MEDFORD,<sup>1</sup> MATTHEW W. HOSEK, JR.,<sup>3</sup> AND SAM ROSE<sup>1,4</sup>

<sup>1</sup>*University of California, Berkeley, Department of Astronomy, Berkeley, CA 94720*

<sup>2</sup>*Observatories of the Carnegie Institution for Science, Pasadena, CA 91101, USA*

<sup>3</sup>*University of California, Los Angeles, Department of Astronomy, Los Angeles, CA 90095*

<sup>4</sup>*Cahill Center for Astronomy and Astrophysics, California Institute of Technology, Pasadena, CA 91125, USA*

(Dated: January 8, 2025)

### ABSTRACT

Gravitational microlensing provides a unique opportunity to probe the mass distribution of stars, black holes, and other objects in the Milky Way. Population simulations are necessary to interpret results from microlensing surveys. The contribution from binary objects is often neglected or minimized in analysis of observations and simulations despite the high percentage of binary systems and microlensing’s ability to probe binaries. To simulate the population effects we added multiple systems to Stellar Population Interface for Stellar Evolution and Atmospheres (SPiSEA), which simulates stellar clusters. We then inject these multiples into Population Synthesis for Compact-object Lensing Events (PopSyCLE), which simulates Milky Way microlensing surveys. When making OGLE observational selection criteria, we find that 55% of observed microlensing events involve a binary system. Specifically, 14.5% of events have a multiple-lens and single source, 31.7% have a single lens and a multiple-source, and 8.8% have a multiple-lens and a multiple-source. The majority of these events have photometric lightcurves that appear single and are fit well by a single-lens, single-source model. This suggests that binary source and binary lens-binary source models should be included more frequently in event analysis. The mean Einstein crossing time shifts from 19.1 days for single events only to 21.3 days for singles and multiple events, after cutting binary events with multiple peaks. The Einstein crossing time distribution of singles and single-peaked multiple events is better aligned with observed distributions from OGLE (Mróz et al. 2017) than singles alone, indicating that multiple systems are a significant missing piece between simulations and reality.

*Keywords:* Gravitational lensing, Binary lens microlensing, Binary source microlensing, Astrophysical black holes, Stellar mass black holes

### 1. INTRODUCTION

Gravitational lensing is when a mass, such as a black hole or star, acts as a lens and bends the light of a background star, magnifying it and creating multiple images. In microlensing we are not able to resolve the individual images, so instead we can see a characteristic brightening and dimming of the source star (Paczynski 1986; Griest et al. 1991). Gravitational microlensing is a powerful phenomenon which we can use for a variety of applications. It can be used to answer Galactic structure questions (Rich 2013) such as the existence of a Galactic bar (Kiraga & Paczynski 1994;

Hamadache et al. 2006; Moniez et al. 2017) and whether the Milky Way’s potential is triaxial (Zhao 1996). It can constrain the population of objects in the Galactic bulge such as dwarf stars which act as lensed sources (Bensby et al. 2013) and the Initial Mass Function of the Bulge (Wegg et al. 2017). It also has the ability to probe the mass distribution of dim objects in the Milky Way, such as exoplanets (e.g. Griest & Safizadeh 1998; Bennett et al. 2008; Gaudi 2012; Penny et al. 2019), brown dwarfs (e.g. Park et al. 2013; Street et al. 2013), and black holes (e.g. Bennett et al. 2002; Mao et al. 2002; Lu et al. 2016; Kains et al. 2018; Wyrzykowski et al. 2019; Wiktorowicz et al. 2019; Wyrzykowski & Mandel 2020).

For isolated black holes in particular, since microlensing only depends on their gravitational nature and does not require them to interact or be in a binary system, microlensing

is the only method to probe them. There is one isolated black hole candidate that has been identified via microlensing (Lam et al. 2022; Sahu et al. 2022; Mróz et al. 2022; Lam & Lu 2023). The mass of only a few dozen other black holes have been measured, all of which were in binaries. These include X-ray binaries (Corral-Santana et al. 2016), merging black holes whose gravitational waves were detected by the Laser Interferometer Gravitational-Wave Observatory (LIGO) (Abbott et al. 2016), and non-interacting black holes in binaries found via their astrometric signals (El-Badry et al. 2023a,b; Chakrabarti et al. 2023). To interpret these findings and put them in a broader astrophysical context, we need to understand the mass distribution, binary fraction, and velocity distributions for all black holes. Uncovering the underlying distribution of black holes in the Milky Way is important to understand the process of stellar evolution, supernovae, potential seeds for super massive black holes at the center of galaxies, and could even give insight into the nature of dark matter.

Numerous photometric surveys have been used to find microlensing events. Historically, the MACHO (Alcock et al. 2000a) and EROS (Tisserand et al. 2007) projects were used to search for dark matter candidates in the Galactic halo through microlensing. More recently, surveys mainly targeting the Galactic bulge are primarily focused on exoplanet microlensing (i.e. OGLE (Udalski et al. 2015), MOA (Sumi et al. 2003), KMTNet (Kim et al. 2018)). There are also other surveys which are not exclusively focused on microlensing which have been used to discover microlensing events (i.e. Gaia (Wyrzykowski et al. 2023), ZTF (Rodriguez et al. 2022; Medford et al. 2023; Zhai et al. 2023), and VVV (Navarro et al. 2020; Husseiniova et al. 2021; Kaczmarek et al. 2022, 2023)). Combined, these surveys find thousands of events each year.

When interpreting these microlensing events, multiple systems have been neglected except when they produce an obvious signal; however, most stars are in multiple star systems (e.g. Duchêne & Kraus 2013). There are some physical phenomena which require the presence of multiple systems, including the production of hypervelocity stars (Rasskazov et al. 2019), and some which require including multiple systems in our interpretations, such as the occurrence rates of exoplanet observations (Moe & Kratter 2021). As such, it is critical to include them when interpreting microlensing surveys, both on the individual event level and population level. As we explore in this paper, the inclusion of multiples can significantly affect the inferred event rates and distributions of microlensing event parameters.

The rest of the paper is organized as follows. In Section 2, we explain how we add binary and triple systems into our microlensing simulation. In Section 3, we detail how the simulations were run and what observational cuts we make

to compare them to data. In Section 5, we discuss our results including the fraction of microlensing events we find, how the Einstein crossing time distribution and event rates compare to observational data, the properties of multiple systems before and after microlensing, and how adding multiple systems affects black hole astrometric candidate selection. In Section 6, we compare our analysis to other simulations and discuss further improvements. In Section 7, we summarize our conclusions.

## 2. ADDING MULTIPLE SYSTEMS TO SPISEA AND POPSYCLE

In Section 2.1, we describe the parameters of binaries input into Stellar Population Interface for Stellar Evolution and Atmospheres (SPISEA, Hosek et al. 2020), a population synthesis code used to generate single-age, metallicity clusters. The companion objects are then injected into Population Synthesis for Compact-object Lensing Events (PopSyCLE, Lam et al. 2020) and we carry out a mock-microlensing survey including these multiple systems, as described in Section 2.2. There were a number of additional improvements made to PopSyCLE. See the PopSyCLE change log for more details.<sup>1</sup>

### 2.1. Binary population parameters

SPISEA is a population synthesis code that generates a star cluster with customizable age, metallicity, and stellar evolution, among other characteristics. The initial version of SPISEA (Hosek et al. 2020) only modeled unresolved stellar multiplicity and its effect on synthetic photometry. In this work, we add functionality to model resolved stellar multiplicity by adding semi-major axis, eccentricity, and orbital parameters for individual systems (see Table 1).

SPISEA has a default or tunable mass-dependent multiplicity fraction, companion star frequency, and mass ratio (Hosek et al. 2020; see also Lu et al. 2013). In SPISEA, the primary is drawn from the initial-mass function (IMF) and is the object with the largest initial mass in the system and the companions are the other less massive objects in the system.

The multiplicity fraction (MF) is the fraction of systems with multiple stars which is a function of the primary mass ( $M$ , in solar masses):

$$MF(M) = AM^\alpha, \quad (1)$$

where  $A = 0.44$  and  $\alpha = 0.51$  by default (Lu et al. 2013). The companion star fraction (CSF) is the number of stars per multiple system which is also a function of mass:

$$CSF(M) = BM^\beta, \quad (2)$$

where  $B = 0.5$  and  $\beta = 0.45$  by default (Lu et al. 2013). In SPISEA we can set a probabilistic or hard limit on the number

<sup>1</sup> <https://popsycle.readthedocs.io/en/latest/source/changelog.html>

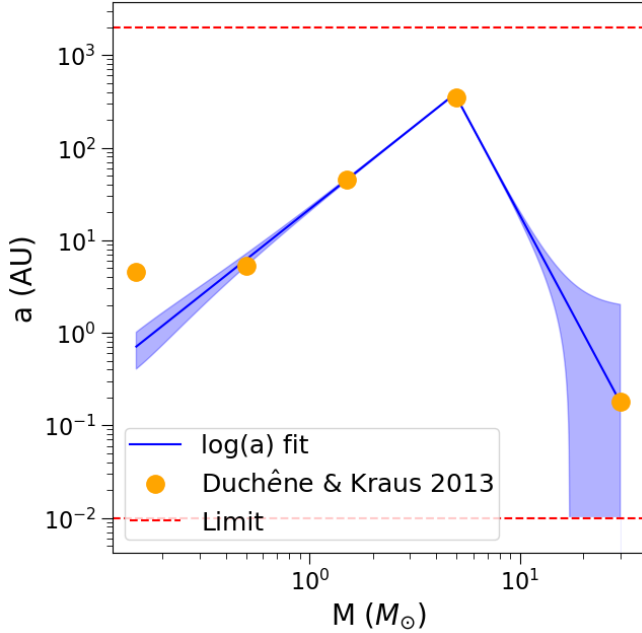


**Figure 1.** Semi-major axis ( $a$ ) as a function of primary mass ( $M$ ). The orange points are the mean semi-major axis values averaged over mass bins in Duchêne & Kraus (2013). We fit these points and corresponding standard deviations, shown in blue. At each mass, the semi-major axis distribution is modeled as a log-normal distribution with a mean (indicated by the dark blue line) and standard deviation (indicated by the shaded blue region). They were fit as a broken power law described in Equation 5. We set a lower limit of  $10^{-2}$  AU (see Fig. 2 of Duchêne & Kraus 2013) and an upper limit of 2000 AU (see Table 2 of Duchêne & Kraus 2013).

of companions per system. To assign each companion mass, SPISEA selects from a distribution of mass ratios,  $q$ , where

$$q = \frac{M_{\text{companion}}}{M_{\text{primary}}}. \quad (3)$$

The default mass-ratio probability density function is:

$$P(q) = q^\gamma, \quad \text{for } q_{\min} \leq q \leq 1, \quad (4)$$

where  $\gamma = -0.4$  and  $q_{\min} = 0.01$  by default (Lu et al. 2013; Kobulnicky & Fryer 2007; Kiminki & Kobulnicky 2012). Note that many of these parameters and relations are uncertain. We allow all of these parameters which are set by default to be changed by the user.

The default resolved properties for the SPISEA multiple star system populations are drawn from observations of the local solar neighborhood.

Duchêne & Kraus (2013) summarize that the frequency of semi-major axes often follows a log normal distribution whose parameters depend on mass, particularly for systems with a lower mass primary star. However, A-type stars were described as having a bimodal distribution and OB-type as a peak with a power law tail. We characterize the separation of

multiples as a log-normal distribution with a mean and standard deviation changes with mass.

We fit the mean semi-major axis vs. mass as a broken power law,

$$a(M) = \begin{cases} A(M/M_{\text{break}})^{-\alpha_1} & M < M_{\text{break}} \\ A(M/M_{\text{break}})^{-\alpha_2} & M > M_{\text{break}} \end{cases} \quad (5)$$

where  $A = 379.8$  AU,  $M_{\text{break}} = 4.9 M_\odot$ ,  $\alpha_1 = -1.8$ , and  $\alpha_2 = 4.2$ . We also limit the maximum separation to 2000 AU (Duchêne & Kraus 2013). We fit the standard deviation of the log of the semi-major axis as a line,

$$\sigma_{\log_{10}(a)} = m \log_{10}(M) + b \quad (6)$$

where  $M$  is in  $M_\odot$ ,  $a$  is in AU,  $m = 0.84$ , and  $b = 0.31$  (see Fig. 1). Since the most massive stars are not described by a log normal in Duchêne & Kraus (2013), we set any objects  $M > 2.9M_\odot$  to  $\sigma_{\log(a)}(2.9M_\odot)$  (where  $2.9M_\odot$  is the lower mass limit of A-type stars) since extrapolating upwards in mass leads to excessively large dispersion in  $a$ .

For the eccentricity distribution, it is unclear if the binaries follow a Maxwellian “thermal” distribution ( $f(e) = 2e$ ) or a flat one ( $f(e) = \text{constant}$ ). A thermal distribution would imply significant interaction between the objects in the binary and their environment so they are able to “thermalize.” A flat distribution would imply more isolated evolution and time to circularize. Duchêne & Kraus (2013) summarize that binaries with  $0.5 \text{ AU} \lesssim a \lesssim 10 \text{ AU}$  are consistent with a flat distribution. Though it is also possible that there is a mass dependent distribution in which less massive primaries have a flatter eccentricity distribution and more massive primaries have a more thermal one (Moe & Di Stefano 2017). Eccentricities of wider binaries have been measured with Gaia; Tokovinin (2020) and Hwang et al. (2022) found closer binaries have a more uniform distribution and wider binaries have a more thermal or even superthermal distribution. In this paper we will use the thermal distribution with  $0 \leq e \leq 1$  and will explore more complex eccentricity distributions in future work.

The rest of the orbital parameters are determined with standard Keplerian distributions.  $i$  is the inclination of the system, which is how tilted the system is with respect to the plane.  $\Omega$  and  $\omega$  describe the orientation of the tilted system in the plane, where  $\Omega$  is the angle of the system around the reference plane and  $\omega$  is the angle between periaapsis and the reference plane in the plane of the system. If  $i$  were  $90^\circ$ ,  $\omega$  would be perpendicular to the reference plane. The frequency of inclination was assumed to be flat in  $\cos(i)$ , and  $\omega$  and  $\Omega$  were both assumed to be isotropic. See Table 1 for a summary.

The stars in SPISEA are then evolved with an Initial-Final Mass Relation (IFMR) which determines whether a star becomes a white dwarf, neutron star, or black hole. Rose et al.

(2022) explores the impact of metallicity-dependent and independent IFMRs in SPISEA and PopSyCLE. In this paper we use a metallicity-dependent IFMR based on the simulations of Sukhbold & Woosley (2014) and Sukhbold et al. (2016) (called SukhboldN20). We leave the inclusion of binary mass exchange, mergers, or ejections to future work (see Section 6.2); however, since stars massive enough to become black holes are all in multiple systems and the objects are evolved independently, the black holes all remain in multiple systems.

## 2.2. Adding multiple systems to PopSyCLE

Population Synthesis for Compact-object Lensing Events (PopSyCLE) performs a population synthesis with a combination of stars from Galaxia and compact objects and multiple system companions from SPISEA. Galaxia, (Sharma et al. 2011) is an implementation of the analytical Besançon model for the Milky Way (Robin et al. 2003), which simulates single stars.

### 2.2.1. Microlensing Terminology

The Einstein radius is the characteristic angular scale in the microlensing event and depends on the mass of the lens ( $M$ ) and distance between the objects ( $d_l$  is the distance between the observer and the lens and  $d_s$  is the distance between the observer and the source):

$$\theta_E = \sqrt{\frac{4GM}{c^2} \left( \frac{1}{d_l} - \frac{1}{d_s} \right)}. \quad (7)$$

The Einstein crossing time is how long it takes for the source to cross the Einstein radius:

$$t_E = \frac{\theta_E}{\mu_{\text{rel}}}, \quad (8)$$

where  $\mu_{\text{rel}}$  is the relative proper motion between the source and lens.

The Einstein radius and Einstein crossing time are both proportional to the square root of the mass of the lens, so more massive lenses result in longer microlensing events and a larger cross-sectional area. For events with multiple system lenses,  $t_E$  can be approximated by using the system mass (primary mass + companion masses) of the lens. For events with multiple system sources, the  $t_E$  definition is unchanged (see Table 10 for a detailed breakdown). The projected heliocentric source-lens separation defined in units of  $\theta_E$  is:

$$u(t) = \sqrt{u_0^2 + \left( \frac{t - t_0}{t_E} \right)^2}, \quad (9)$$

where  $u_0$  is the closest lens-source separation in units of  $\theta_E$ ,  $t_0$  is the time of closest approach between the source and lens,

and  $t$  is the time of observation. The amplification of the source is a function of  $u$ :

$$A(t) = \frac{u^2 + 2}{u \sqrt{u^2 + 4}}, \quad (10)$$

and is maximized when  $u = u_0$ . The light from the source is often blended with nearby objects in the seeing disk which can contaminate light from the source. The blend source flux fraction is defined as:

$$b_{\text{sf}} = \frac{F_S}{F_S + F_L + F_N} \quad (11)$$

where  $F_S$  is the flux of the source,  $F_L$  is the flux of the lens, and  $F_N$  is the flux of the neighbors or nearby objects in the seeing disk. When  $b_{\text{sf}} = 1$ , the event is totally unblended and flux is only observed from the source, and maximum blending is achieved when  $b_{\text{sf}}$  approaches zero.

The bump magnitude ( $\Delta m$ ) is the difference between the peak magnitude and baseline magnitude:

$$\Delta m = -2.5 \log_{10} \left( \frac{A(t_0) F_S + F_L + F_N}{F_S + F_L + F_N} \right). \quad (12)$$

These equations do not take into account the motion of the Earth around the Sun. As Earth orbits, our perspective on the event changes. We can measure this microlensing parallax signal defined as:

$$\pi_E = \frac{\pi_{\text{rel}}}{\theta_E} \quad (13)$$

where  $\pi_{\text{rel}}$  is the relative parallax between the source and lens:

$$\pi_{\text{rel}} = (1 \text{ AU}) \left( \frac{1}{d_l} - \frac{1}{d_s} \right). \quad (14)$$

This signal may manifest in asymmetry and additional peaks in the light curve.

Combining Eqs. 7, 13, and 14 yields an estimate of the lens mass:

$$M = \frac{\theta_E}{\kappa \pi_E} \quad (15)$$

where  $\kappa \equiv \frac{4G}{(1 \text{ AU})c^2}$ .  $\pi_E$  is routinely measured with photometric light curves for microlensing events with  $t_E > 100$  days; however,  $\theta_E$  measurements are rare and require astrometric measurements or detection of finite source effects.

In microlensing events, the multiple-system can be the lens, source, or both. These are referred to as point source-binary lens (PSBL), binary source-point lens (BSPL), and binary source-binary lens (BSBL), respectively. When there is no binary, this is referred to as point source-point lens (PSPL). See Table 10 for additional details.

### 2.2.2. Adding Companions to PopSyCLE

Multiples are added to the population synthesis aspect of the code in two different ways since the stars are from

**Table 1.** Binary table parameters

Column	Description	Units	SPISEA	PopSyCLE
log(a)	Log of the system semi-major axis	AU	×	×
e	Eccentricity	–	×	×
i	Inclination	Degrees	×	×
$\Omega$	Longitude of ascending node	Degrees	×	×
$\omega$	Argument of periapsis	Degrees	×	×
P	Period	Days		×
$\alpha$	Angle between North and binary axis (East of North)	Degrees		×
$\phi_{\pi_E}$	Angle between North and relative proper motion (East of North)	Degrees		×
$\phi$	Angle between binary axis and relative proper motion	Degrees		×

NOTE—These are the additional parameters added to SPISEA companion and PopSyCLE companion output tables. See Table 2 in Hosek et al. (2020) for the rest of the columns. × in the SPISEA column indicates that the parameter is available in SPISEA (see Section 2.1 for more details) and × in the PopSyCLE column indicates that the parameter is available in PopSyCLE (see Section 2.2.3 for more details).

Galaxia and compact objects and injected from SPISEA. For each PopSyCLE age and metallicity bin, a SPISEA cluster is generated with the appropriate mass containing both compact objects and stars with a maximum of two companions. The IMF of the primaries is from Galaxia which has different IMFs for each of the major stellar populations (e.g. bulge, disk halo) (see Sharma et al. 2011, Table 1). The matching clusters in SPISEA are drawn from a Kroupa mass function, which is used to populate all compact objects; however, the intrinsic Galaxia mass function for stars is preserved through mass-matching, as described in Lam et al. (2020), Section 3.

As before, the SPISEA compact objects are added to the PopSyCLE population of stars already generated from Galaxia. Any companions to compact objects are also injected from SPISEA into the PopSyCLE population.

We then match SPISEA primary stars with Galaxia stars by mass. A summary of this matching process can be seen in Fig 2. We do so by making a KDtree of the Galaxia star masses and search the tree iteratively for SPISEA primary mass matches requiring the following:

- $M_{\text{Galaxia}} > M_{\text{SPISEA}}$  to ensure that  $q$  remains  $< 1$
- $(M_{\text{Galaxia}} - M_{\text{SPISEA}})/M_{\text{Galaxia}} < 0.2$
- Unique matches

where  $M_{\text{Galaxia}}$  is the ZAMS mass of the star from Galaxia and  $M_{\text{SPISEA}}$  is the ZAMS mass of the primary star from SPISEA. We continue to iteratively search for the nearest neighbors in mass if any of the above criteria are unmet. We remove all systems with  $(M_{\text{Galaxia}} - M_{\text{SPISEA}})/M_{\text{Galaxia}} > 0.2$  to the nearest neighbor and systems where  $M_{\text{SPISEA}} >$

$\max(M_{\text{Galaxia}})$ , which affects 0-5% of systems. We then associate the SPISEA companions with the Galaxia stars so that the Galaxia stars replace the SPISEA primary stars.

The microlensing event calculation aspect of the program is modified in the following ways:

- Event  $t_E$ ,  $u_0$ ,  $\theta_E$ , maximum magnification, and bump magnitude ( $\Delta m$ ) are now calculated using the total system mass defined as  $M_{\text{sys}} = \sum_{i=1}^{N_{\text{obj}}} M_i$  where  $N_{\text{obj}}$  is the number of objects in the system (i.e.  $N_{\text{obj}} = 3$  for triples).
- All magnitudes in primary and event tables are system luminosities that include flux contributions from the primary and any companions for the system. The system luminosity is used to calculate the  $b_{\text{sf}}$  values.
- The search radius is increased from  $n\theta_E$  (where  $n$  is a user specified parameter defaulting to 2) to  $(n\theta_E) + a \sin(i)$  (where  $a \sin(i)$  is the projected binary separation). PopSyCLE continues to use the position of the primary for the center of the search radius for candidate events. Since the projected separation between the binary lenses was found to be larger than  $\theta_E$  approximately 50% of the time, we extend the candidate radius to find all potential events.

### 2.2.3. Available Binary Parameters

We calculate binary parameters for each companion in every system including multiple lenses and sources. The following parameters are calculated so binary light curves can be simulated later: the current mass ratio between the companion and primary star ( $q$ ), projected separation in milliarcseconds, period in years, and three binary angles:  $\alpha$ ,  $\phi_{\pi_E}$  and  $\phi$  (see explanation below and Eqs. 17-19).

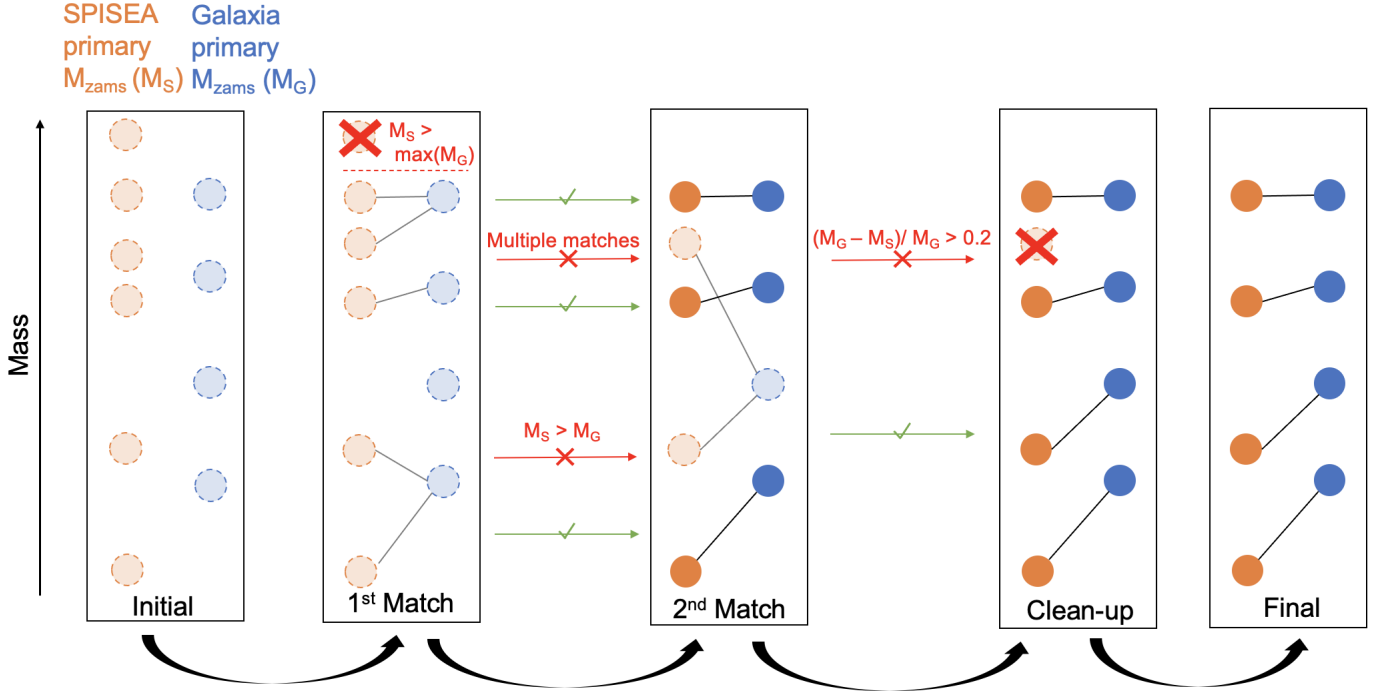


**Figure 2.** We show the matching process of the Galaxia stars and SPiSEA primary stars. The orange circles represent SPiSEA primary stars and the blue circles represent Galaxia stars. Circles with a dotted boarder and faint color represent unmatched objects and filled in circles represent objects with a confirmed match. Lines drawn between dotted circles are tentative matches which are either confirmed or rejected indicated with a green line with a checkmark or a red line with an x, respectively. The text above the red line indicates why the match was rejected. The circles are ordered so those with the smallest ZAMS mass are at the bottom and the largest ZAMS mass are at the top. From left to right, the first panel shows the initial configuration of the objects. The second panel shows the first set of matches where the SPiSEA stars are matched to the nearest Galaxia star in mass. Any SPiSEA stars more massive than the most massive Galaxia star are eliminated. Three of the matches shown are accepted and two are rejected. The upper match is rejected since there are multiple SPiSEA stars matched to the same Galaxia star, so the further object is rejected. The lower match is rejected since the SPiSEA mass is larger than the Galaxia mass - this criteria is to ensure that  $q$  remains  $< 1$ . In the third panel, the SPiSEA stars that are still unmatched are matched to the next closest Galaxia star in mass. One match is accepted and the other is rejected since the closest Galaxia star mass is further than 20% away from the remaining SPiSEA star. In the fourth panel, there are no more unmatched Galaxia stars and the final SPiSEA star is eliminated. The final configuration of matches is shown on the right.

The period in years is calculated using Kepler's third law:

$$P = \sqrt{\frac{4\pi^2 a^3}{GM}}, \quad (16)$$

where  $a$  is the separation in AU and  $M$  is the total mass of the system in  $M_\odot$ .

$\alpha$  is the angle between the binary axis and North (East of North). It is calculated as:

$$\alpha = \tan^{-1} \left( \frac{\Delta z_{RA\cos(\text{Dec})}}{\Delta z_{\text{Dec}}} \right) - 180^\circ \quad (17)$$

where  $\vec{\Delta z} = (\Delta z_{RA\cos(\text{Dec})}, \Delta z_{\text{Dec}})$  is the position of the companion with respect to the primary as calculated in Section 2.2.4 and  $\tan^{-1}$  is the arctan2 function which returns angles between  $-\pi$  and  $\pi$  radians.  $180^\circ$  is subtracted off to point the vector towards the primary instead of towards the companion.

$\phi_{\pi_E}$  is the angle between the vector of North and the relative proper motion between the source and the lens ( $\vec{\mu}_{rel}$ ), measured as East of North. This is calculated as:

$$\phi_{\pi_E} = \tan^{-1} \left( \frac{\mu_{rel,RA\cos(\text{Dec})}}{\mu_{rel,Dec}} \right) \quad (18)$$

$\phi$  is the angle between the binary axis and the proper motion vector where the binary axis points towards the primary. It can be calculated from  $\alpha$  and  $\phi_{\pi_E}$ :

$$\phi = \alpha - \phi_{\pi_E} \quad (19)$$

#### 2.2.4. Orbital Mechanics

We assume a static binary over the entire microlensing survey window (i.e. no orbital motion). The static position is sampled from the orbit using a random orbital phase. We calculate  $\vec{\Delta z}$ , the position of the companion with respect to the primary using: the orbital parameters  $\omega$ ,  $\Omega$ ,  $i$ , and  $e$  (see

the end of Section 2.1); the orbital period ( $P$ ), the semi-major axis ( $a$ ), and the mass of the primary ( $M$ ); and an initial time  $t_{\text{init}} = nP + t_0$ , where  $n$  is a random number between 0 and 1. Following the equations outlined in Van De Kamp (1967) and applied in Lu et al. (2009), we first calculate the following Thiele-Innes constants:

$$A = a(\cos \omega \cos \Omega - \sin \omega \sin \Omega \cos i) \quad (20)$$

$$B = a(\cos \omega \sin \Omega + \sin \omega \cos \Omega \cos i) \quad (21)$$

$$F = a(-\sin \omega \cos \Omega - \cos \omega \sin \Omega \cos i) \quad (22)$$

$$G = a(-\sin \omega \sin \Omega + \cos \omega \cos \Omega \cos i) \quad (23)$$

The eccentricity anomaly ( $E$ ), which describes where the object is in an elliptical orbit at  $t_{\text{init}}$ , is calculated numerically (see Lu et al. 2009). Then it is used to calculate the elliptical rectangular coordinates:

$$X = \cos E - e \quad (24)$$

$$Y = \sqrt{1 - e^2} \sin E. \quad (25)$$

The derivative of  $E$  is:

$$\dot{E} = \frac{\bar{m}}{1 - e \cos E}, \quad (26)$$

where  $\bar{m}$  is the mean motion in radians per year:

$$\bar{m} = 2\pi/P. \quad (27)$$

These are then used to find the projected positions and velocities with respect to the primary:

$$z_E = BX + GY \quad (28)$$

$$z_N = AX + FY \quad (29)$$

where  $z$  is in AU. When modeling lightcurves we assume a static binary. In the future we will incorporate orbital motion into the microlensing event; however, this would significantly add to run time (see Section 6.2).

### 2.2.5. Binary Light Curves

Previously in PopSyCLE, the user would determine whether an event is detectable using the baseline magnitude,  $u_0$ , and  $\Delta m$  at closest approach. However, for binary and triple systems, the point of maximum magnification may not correspond to the closest approach to the primary. To properly determine detectability for multiple systems, we simulate lightcurves for all the events that contain a multiple system and store the parameters. In the case of triple lenses/sources, we simulate multiple binary lightcurves with each primary-secondary pair and choose the one with the largest amplitude (see Appendix B for details). See Appendix C for an analysis on the relative effect of triple systems, but in this analysis, we leave fully simulating the triple systems to future work (see Sec. 6.2).

The following parameters were then calculated for each event:

1. Number of peaks ( $n_p$ ) in the light curve defined with a prominence of at least  $10^{-5}$  magnitudes by `scipy.find_peaks()`. The prominence is defined as the minimum height needed to descend from the peak until a higher peak's baseline is reached, where a peak is a local maxima in magnitude space (lowest magnitude).  $10^{-5}$  is far in excess of what is detectable by current ground based observatories; however, we cut based on this later and chose this value to allow for future flexibility.
2. Bump magnitude defined as the maximum magnitude - minimum magnitude. For an event with a single peak, the prominence is equivalent to the bump magnitude.
3. Time at which the highest peak occurs.
4. Average of the  $n_p$  times at which the peaks occur.
5. Standard deviation of the  $n_p$  times at which the peaks occur.

For events with more than one peak, we calculate the following parameters for each peak in a separate table:

1. Time at which the peak occurs.
2. Bump magnitude of that peak, defined as the maximum magnitude of the peak - minimum magnitude of peak. ( $\Delta m$ )

For additional parameters see PopSyCLE documentation.<sup>2</sup>

## 3. POPSYCLE SIMULATIONS

We ran PopSyCLE simulations for eighteen fields each with area  $0.34 \text{ deg}^2$ . As we compare the results to the OGLE IV Microlensing Survey (Udalski et al. 2015), we chose fields to correspond with OGLE IV fields which are listed in Table 2. The simulations are publicly available.<sup>3</sup>

These fields were simulated in the I filter with a  $0.65''$  blend radius to mimic OGLE's median seeing of  $1.3''$  (see Section 4 of Lam et al. 2020). The Galactic parameters used correspond to `Galaxia v3` (see Appendix A of Lam et al. 2020). We did two sets of simulations where we will call runs with multiples M Runs (multiples runs) and runs without S Runs (singles runs).

For the simulations, we used extinction as described in Lam et al. (2020) which uses the Schlegel et al. (1998) E(B-V) values from which `Galaxia` produces an estimated integrated 3D dust map and the Damiani et al. (2016) reddening

<sup>2</sup> <https://popsycle.readthedocs.io/en/latest/>

<sup>3</sup> <https://w.astro.berkeley.edu/popsycle/>

**Table 2.** Fields run in PopSyCLE

Field Name	$\ell$	$b$
BLG 500	1.00°	-1.03°
BLG 501	-0.61°	-1.64°
BLG 504	2.14°	-1.77°
BLG 505	1.09°	-2.39°
BLG 506	-3.00°	0.01°
BLG 507	-1.06°	-3.61°
BLG 511	3.28°	-2.52°
BLG 512	2.22°	-3.14°
BLG 527	8.81°	-3.64°
BLG 534	-1.14°	-2.25°
BLG 535	-2.21°	-2.86°
BLG 629	7.81°	4.81°
BLG 611	0.33°	2.82°
BLG 645	3.20°	-1.15°
BLG 646	4.34°	-1.90°
BLG 648	1.96°	0.94°
BLG 652	1.85°	2.30°
BLG 675	0.78°	1.69°

NOTE—This is the list of fields simulated and analyzed. The first column is the name, which “BLG #” correspond to the name “OGLE-IV-BLG#”. The second column is galactic longitude,  $\ell$ . The third column is galactic latitude,  $b$ . Each field has an area of 0.34 deg<sup>2</sup>.

law. See Lam et al. (2020) Appendix B for CMDs compared to OGLE.

Microensing events were identified using observability criteria to match the limits of OGLE observations. See Table 3 for a summary of cuts that were made to mock results. Unless otherwise specified, we use Mock OGLE Early Warning System (EWS, Udalski et al. 2015) cuts. For OGLE EWS we required  $I_{\text{base}} \leq 21$ , an  $I$ -band bump magnitude of  $\geq 0.1$ , and  $|u_0| \leq 2$ . The bump magnitude ( $\Delta m$ ) cut is made to remove low amplitude events (Lam et al. 2020). For events containing a multiple system, the bump magnitude was calculated from the simulated binary light curves (see Section 2.2.5). Multiple-lens events are only counted as multi-peak if the secondary peak has  $\Delta m \geq 0.02$ . This is an estimate based on the mean OGLE uncertainty (see Fig. 2 of Skowron et al. 2016), since if a primary peak is identified, the light curve will be scrutinized more carefully for secondary peaks. This does not take into account gaps from cadence, though. In

**Table 3.** Mock Microlensing Cuts

	Mock EWS	Mock Mróz17	Mock Mróz19
Filter	I	I	I
Source Mag	–	$\leq 22$	$\leq 21$
Baseline Mag	$\leq 21$	–	–
$\Delta m$	$\geq 0.1$	–	–
$ u_0 $	$\leq 2$	$\leq 1$	$\leq 1$

NOTE—This table is a summary of the cuts made to simulate the OGLE Early Warning System (EWS), Mróz 17 (Mróz et al. 2017), and Mróz 19 (Mróz et al. 2019). When comparing specifically with OGLE numbers, we make the additional cut of one observable peak, where the second peak must have  $\Delta m \geq 0.02$  to be considered observable.

order to do so, we fit the microlensing events with an OGLE-like cadence as described in Section 4.

#### 4. FITTING SIMULATED LIGHTCURVES

As a post-processing step, we generated OGLE-like photometry for the 5,898 microlensing events that passed Mock EWS cuts (see Table 3), including both PSPL and multiple events, and fit them with PSPL models using BAGLE (Bayesian Analysis of Gravitational Lensing Events)<sup>4</sup>.

We created realistic temporal sampling for each PopSyCLE light curve by selecting a real OGLE lightcurve from 2016 from each field from the OGLE EWS webpage and giving all the lightcurves from that field the cadence that matched that real lightcurve. There were no lightcurves alerted for field BLG 629 in 2016, so we chose a lightcurve from a neighboring field, BLG 630 for those lightcurves. We shifted the simulated  $t_0$  values from PopSyCLE (which are between -500 and 500) by 56400 days, which is the midpoint in MJD of the available timeseries of the lightcurves. We generated errorbars for the lightcurves by fitting the errors of 100 randomly selected lightcurves from the dataset provided in Mróz et al. (2019). We found the following best fit flux-mag relation and flux errors:

$$F = 350 \text{ counts} \times 10^{\frac{m-16}{-2.5}} \quad (30)$$

$$F_{\text{err}} = F^{0.85} \quad (31)$$

We also added Gaussian scatter with an amplitude the size of the errorbars.

Next we fit the simulated lightcurves with point-source, point-lens models. We fit the events to assess, in more detail, what fraction of multiple events may be mistaken for PSPL and to understand biases in parameters that may be caused

<sup>4</sup> [https://github.com/MovingUniverseLab/BAGLE\\_Microlensing/tree/main](https://github.com/MovingUniverseLab/BAGLE_Microlensing/tree/main)



**Table 4.** Simulated Event Priors

Parameter	Prior
$t_E$	$\mathcal{U}(0, 400)$
$t_0$	$\mathcal{U}(55200, 57700)$
$u_0$	$\mathcal{U}(-1, 1)$
$m_{\text{base}}$	$\mathcal{U}(m_{\text{base, sim}} - 0.5, m_{\text{base, sim}} + 0.5)$
$b_{\text{sf}}f$	$\mathcal{U}(0.001, 1.25)$

NOTE—These are the priors used for fitting the lightcurves that passed the OGLE EWS cuts using BAGLE, the procedure of which is described in Section 4. We chose the  $t_0$  ranges to be the approximate minimum and maximum dates in MJD of the real OGLE EWS timeseries we used. We allow  $b_{\text{sf}}f$  to be above 1 to accommodate for “negative blending” which can occur due to systematics in background subtraction (e.g. Smith et al. 2007).

by fitting events with multiples with PSPL models. We do not include parallax to match the methodology of the current ground based surveys which do not fit parallax except when the lightcurves fit poorly by a PSPL without parallax fit. We use priors as described in Table 4. We used BAGLE to do the fitting which uses `pymultinest` nested sampling algorithm. This can be beneficial in a degenerate parameter space like microlensing in which one can often have multimodal solutions. Another benefit to using this fitting algorithm is that we have full posteriors for the microlensing events we fit which can be used for future statistical studies.

Once we fit the lightcurves, we eliminated those that did not deviate significantly from a “straight line fit” (the sigma-clipped ( $3\sigma$ ) mean of the lightcurve). This was determined by calculating the reduced  $\chi^2_{\text{const}}$  values for each lightcurve and eliminating those that were below the 99th percentile of the corresponding reduced  $\chi^2$  distribution. In equation form, lightcurves that met the following criteria were eliminated:

$$\frac{\chi^2}{dof} < \frac{\chi^2_{0.99}}{dof}. \quad (32)$$

where  $dof$  is the degrees of freedom in the model. This eliminated 72% of lightcurves. These lightcurves either had an event that peaked in a seasonal gap or were faint and had a larger amplitude of scatter than the change in magnitude due to the microlensing event. We then determined which fit well by a PSPL lightcurve. By fit well, this means those with a reduced  $\chi^2_{\text{PSPL}}$  less than the 99th percentile of the corresponding reduced  $\chi^2$  distribution. We will discuss these results in Section 5.3.

## 5. RESULTS

### 5.1. Fraction of Multiple Events

We found that over half of our simulated microlensing events contain a multiple lens, source, or both. These are events that passed Mock-EWS cuts (see Table 3) and should be compared with completeness-corrected OGLE EWS results. The results from the sample of fitted events that pass observability criteria before completeness correction will be discussed in Section 5.3. As can be seen in the left plot of Figure 3 and Table 5, 55% of events that meet Mock OGLE EWS cuts contain a multiple lens or source. Of those, 94.4% of multiple events are single peaked and have the potential of masquerading as a PSPL microlensing event. This leaves 3.1% of all events as obvious, multi-peaked multiple events, as can be seen in the right plot of Fig. 3. 10.4% of all events and 10.1% of single peaked events have at least one triple system; see the caption of Fig. 3 and Appendix C for details.

We also investigated the flux ratios of the binaries to probe the fraction with a secondary component that contributes significantly to the flux. We found that 37% have a fainter component which contributes at least 10% of the system flux and 6% have a fainter component which contributes at least 40% of the flux. Hence, most systems have one component of the binary source which is significantly brighter than the other and is consistent with Fig. 3 and Table 5, indicating that most binary source events appear as singles. While this is true for an OGLE style sample, for upcoming telescopes such as Roman or Rubin which probe to greater depths, these fractions will likely change.

In addition, we find that the fraction of multiple events is dependent on the minimum magnitude the survey is sensitive to. As the magnitude increases and we include fainter stars, the multiple event fraction decreases by a few percent. The multiple event fraction may also be dependent on the wavelength of observation and the resolution, cadence, and photometric precision of the survey. These effects will be studied in future work.

In Fig. 4, we plot randomly selected example microlensing lightcurves classified as true singles, single-peaked multiples, and multi-peaked multiples. The green lightcurves in Fig. 4 are events with a binary source or lens with a single observable peak. While some have a shoulder or some asymmetry, the second peak does not rise above  $\Delta m \geq 0.02$  and others appear visibly indistinguishable from typical PSPL events. There may also be parallax signal in PSPL lightcurves (see the left blue curve in Fig. 4) which may not fit well by a PSPL-no parallax model. Without modeling work that takes into account these higher order effects, one cannot interpret these populations accurately.

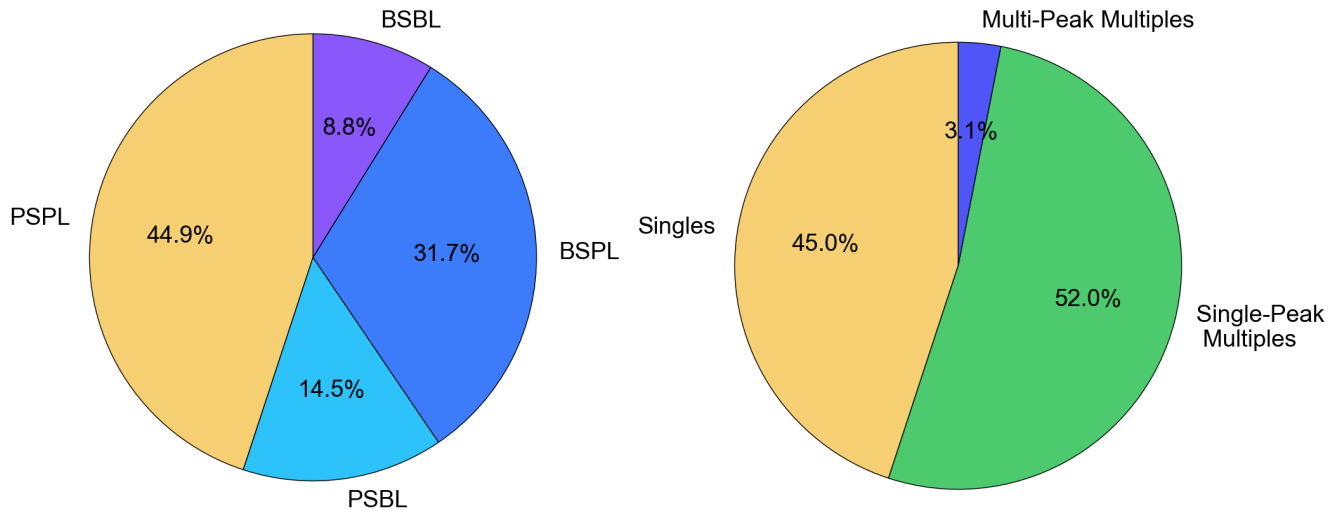


**Figure 3.** *Left* shows the percentage of the intrinsic population with OGLE EWS observability cuts with a single source and single lens (PSPL), a single source and multiple lens (PSBL; 19% of which have a triple lens), a multiple source and single lens (BSPL; 15% of which have a triple source), and multiple source and multiple lens (BSBL; 31% of which have a triple lens or source) as indicated in Table 5, where PSPL events are in yellow and events with a multiple system are in varying shades of blue. We find that more than half of microlensing events include at least one multiple system. This fraction can change depending on the minimum magnitude the survey is sensitive to, the wavelength of observation, and the resolution of the survey (see Section 5.1). *Right* shows the percentage of single (PSPL) events, single-peaked events with at least one multiple system (20% of which have a triple system), and multi-peaked events with at least one multiple system (20% of which have a triple system). We find that most multiple microlensing events have a single peak and have the possibility of being mistaken as a single-only event.

**Table 5.** Breakdown of Multiple Microlensing Events

	Both Multiple	Lens Multiple	Source Multiple	Neither Multiple
% of Total	8.8%	14.5%	31.7%	44.9%
Multipeak % of Total	0.3%	2.6%	0.2%	-
Multipeak % of Category	3.5%	17.8%	0.5%	-

NOTE—This table has the percent of all events where either both the lens and source are multiple systems, just the lens is a multiple system, just the source is a multiple system, or neither are with mock OGLE EWS cuts. ‘% of Total’ is the percentage of total which are multiple systems. ‘Multipeak % of Total’ is the percentage of all events which have multiple peaks from that category; i.e. 2.6% of all events are multi-peaked PSBL events. ‘Multipeak % of Category’ is the percentages of each category which have multiple peaks; i.e. 17.8% of PSBL events are multi-peaked. We find the percentage of single-only events with multiple peaks (which are caused by parallax) to be negligible ( $\sim 0.04\%$ ).

We can also see in Table 5 that most multi-peaked events are PSBL (2.6% of all events). Also, a higher percentage of PSBL events are multi-peaked. 17.8% of PSBL events are multi-peaked, 0.5% of BSPL events are multi-peaked, and 3.5% of BSBL events are multi-peaked. Our simulated percentages of multi-peaked events matches well with the fraction of binary events detected by surveys, with 2-11% of events being determined to be binaries. Most early sur-

veys identified binaries by visual inspection and found 6% binaries (Alcock et al. 2000b), 3-11% binaries (Jaroszynski 2002), 1.8% binary lenses and 1.8% binary sources (Jaroszynski et al. 2004), 3.1% binary lenses and 0.8% binary sources (Jaroszynski et al. 2006), 1.5% binary lenses and 0.7% binary sources (Skowron et al. 2007), 1.5% binary lens and 0.1% binary sources (Jaroszyński et al. 2010). More recent studies have cut out “anomalous” events (i.e. events with large binary and parallax signals) which do not fit well by a PSPL-model with no parallax with a  $\chi^2$  criteria (i.e.  $\chi^2/dof \leq 2$  in Mróz et al. 2019). They then scale up the event rates and optical depths by a factor to account for those which have been removed based on previous established fractions of binary events. They scale assuming a binary fraction of 6% and that contribution to the optical depth of a binary lens is  $\sqrt{2}$  more than a single lens (Sumi et al. 2006, 2013; Mróz et al. 2019), though Mróz et al. (2019) mention they find  $\sim 10\%$  anomalous events. While we can reproduce the fraction of “obvious” binaries that are caught by surveys, this still indicates there is a significant fraction of events with multiples in data which are masquerading as PSPL events. Events with multiple lenses tend to have longer  $t_E$  values than those without (see Fig. 5 and Table 5), so when interpreting  $t_E$  distributions from photometric surveys, it is critical to take multiples into account.

## 5.2. Comparison of PopSyCLE to OGLE data

Adding multiples drove the mean of the Einstein crossing time distribution to a longer time and also led to an increased

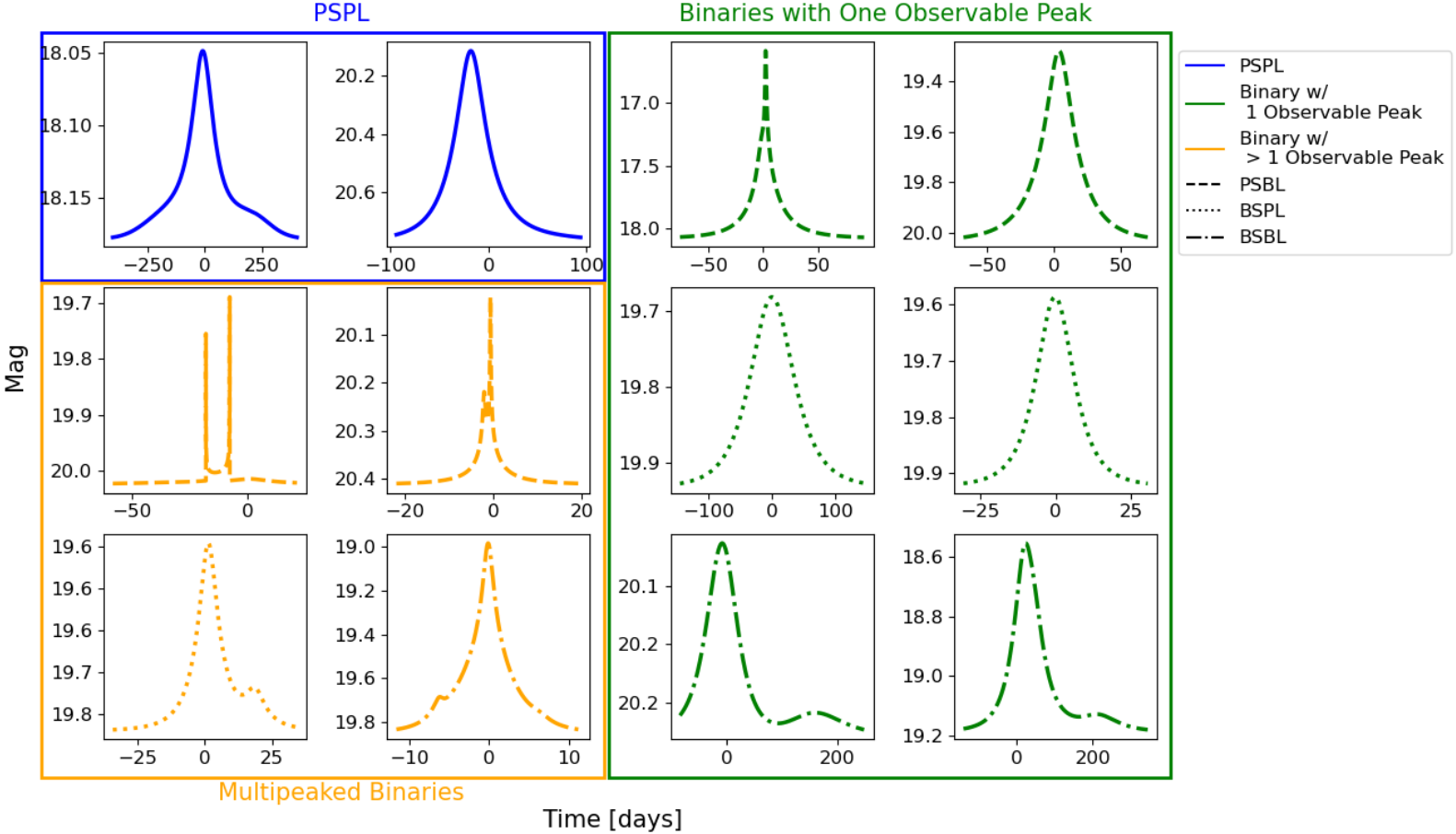


**Figure 4.** This is a set of random example lightcurves from the PopSyCLE simulation where time is in days where 0 corresponds to  $t_0$ . In blue are PSPL events. Deviations from the prototypical microlensing shape in these lightcurves are due to parallax. Binary events with more than one peak are plotted in orange and binary events with one observable peak are plotted in green. Dashed lines indicate PSBL, dotted lines indicate BSPL, and dash-dot lines indicate BSBL. As can be seen in the green plots, some binary events have shoulders or small asymmetries, but others appear indistinguishable from typical PSPL events and therefore may masquerade as PSPL events.

population of events at long  $t_E$ . The mean  $t_E$  increased by 2.6 days and the median  $t_E$  by 1.2 days (see Table 6). A number of these binaries, though, would be unlikely to be mistaken for PSPL events. Those with multiple observable peaks can be cut out. When comparing the single peaked population to singles only, the mean  $t_E$  increased by 2.2 days and the median  $t_E$  increased by 0.9 days.

To compare our  $t_E$  distribution with OGLE, we used the distributions in Mróz et al. (2017) from Extended Data Table 4 corrected with detection efficiencies from Extended Data Table 5. We took the 9 simulated PopSyCLE fields that correspond to the OGLE fields analyzed in that paper and made Mock Mróz17 cuts to match. With single systems only, the peak of PopSyCLE’s  $t_E$  distribution was less than that of the data and the distribution was unmatched at long  $t_E$  values. The presence of multiple systems in the simulation brought our simulated  $t_E$  distribution into better agreement with the observed distribution. We can see this shifted the PopSyCLE distribution into better alignment with the peak and at long

durations with the OGLE distribution (see Fig. 6). Since the PopSyCLE simulation does not include brown dwarfs or exoplanets, we do not expect the distributions to match at  $t_E \lesssim 3$  days.

We performed a Kolmogorov-Smirnov two-sample test between the data from Mróz et al. (2017) and the M Run and S Run data in Fig. 6. We made 1000 realizations of the OGLE distribution and found a mean p value of  $9.34 \times 10^{-4}$  when comparing M Runs and OGLE and  $3.06 \times 10^{-10}$  when comparing S Runs and OGLE.

Adding in multiples also brought the observed field-averaged event rate into better agreement with our simulations. The average between fields can be seen in Table 7 and the individual fields in Table 8. We find that the event rate in events/deg<sup>2</sup>/year is closer and within the errorbars of the data. The  $N_{\text{stars}}/\text{deg}^2$  data has better agreement with M Runs, but events/star/year has better agreement between S Runs and the data (though they are similar within the errorbars), assuming each multiple star system is blended as one star; how-

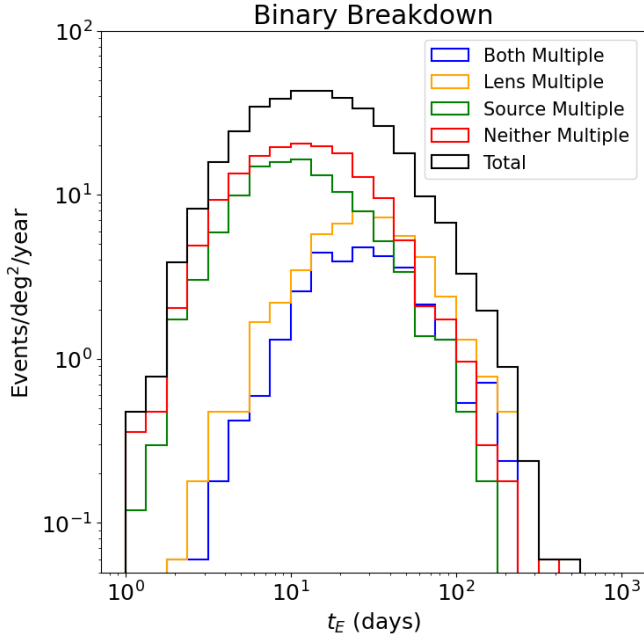


**Figure 5.** Number of events/deg<sup>2</sup>/year as a function of Einstein crossing time (Eq. 8) in days for M Runs. The black distribution is the total, the blue is events where both the lens and source are multiples, yellow is events where only the lens is a multiple, source is events where only the source is a multiple, and red is events where neither are multiples. In general, events with a multiple lens have longer Einstein crossing times than those which do not, which makes sense since companions add mass leading to longer  $t_E$  if the mass is added to the lens. See Table 5 for the percent of each population and Table 6 for the mean and median  $t_E$ .

ever, there is confusion in the number of stars. If stars are blended, this will artificially increase their brightness, which could bring them above the magnitude cut, but also blending will decrease the number of stars that can be distinguished. OGLE efficiency corrects their  $N_{stars}$  with the Hubble Space Telescope (HST) as truth (Holtzman et al. 2006), but we do not attempt to find the number of stars as measurable by HST (where multiple star systems are counted a single blended star), so events/deg<sup>2</sup>/year is the more comparable measurement. See Lam et al. (2020) Appendix A and B for additional comparisons between PopSyCLE and data.

### 5.3. Fitting Lightcurves and Parameter Bias

In Section 4, we described fitting the 5,898 lightcurves that passed the Mock-OGLE EWS cuts. 28% of those had significant signal beyond a straight line (see Section 4). Of those, 91.3% of events were fit well by PSPL models. As can be seen in Fig. 7, 39% of events were PSPL events that were fit well by a PSPL model, 52.4% were multiple event that were fit well by a PSPL model, 1.7% were PSPL events that fit

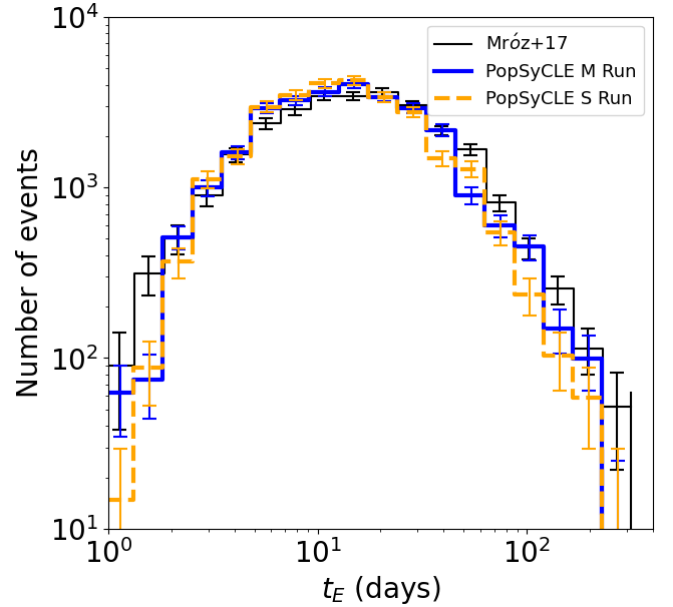


**Figure 6.** Number of events as a function of the Einstein crossing time in days with the distribution of events from S Runs in the yellow dashed line, single and single-peaked multiple events from M Runs in the blue solid line, and event distributions from Mróz et al. (2017) divided by their appropriate detection efficiencies. The simulations are both with OGLE-M17 style cuts (see Table 3). The S Runs and M Runs are each scaled such that the number of events are the same as the data. Only single and single-peaked multiple events are kept for the M Runs since OGLE only includes those they fit as PSPL events in their analysis. The PopSyCLE data is from a subset of fields simulated in Table 2 to match those in Mróz et al. (2017) – they report fields 500, 501, 504, 505, 506, 511, 512, 534, and 611. Neither distribution matches well at the low- $t_E$  end, which is expected due to the lack of brown dwarfs in PopSyCLE. The M Runs match the peak and the long duration events of the OGLE distribution within the errorbars in most cases, more than in the S Run case.

**Table 6.** PopSyCLE Statistics

Type	$\langle t_E \rangle$ (d)	med( $t_E$ ) (d)	$f_{BH}$ at $t_E > 120$ d
S Run	19.1	12.8	0.31
M Run total	21.7	14.0	0.29
M Run Single Peak	21.3	13.7	0.31
M Run Sing Lens	16.8	11.3	0.00
M Run Mult Lens	37.8	27.8	0.38

NOTE—This table has the mean  $t_E$  in days, median  $t_E$  in days, and fraction of lenses that are black holes with  $t_E > 120$  days for a variety of runs and cuts. The first row are the values for S Runs and the rest are for various populations of the M Runs. Each population has Mock OGLE EWS cuts applied as described in Table 3.

**Table 7.** This table compares the field average of singles-only simulations (S Runs) and single-peaked multiples+singles simulations (M Runs) to Mróz et al. (2019) values by making the cuts indicated in Table 3. We average the results across the fields we simulated for the Mróz et al. (2019) results. We compare the number of stars/deg<sup>2</sup> (where multiple star systems are counted a single blended star), events/star/year, events/deg<sup>2</sup>/year and the mean  $t_E$  between 0.5 and 300 days. We also compute the median  $t_E$  between 0.5 and 300 days.  $N_{\text{stars}}$  is  $10^{-6}$  the value in the simulation. We take the average of each of the fields where the errors are the error on the mean. Individual field comparisons can be found in Table 8. We find that adding in multiples brings the field average  $t_E$  into agreement with Mróz et al. (2019). We also find that the  $N_{\text{stars}}/\text{deg}^2$  is closer to the data and event rate in events/deg<sup>2</sup>/year is closer and within the errorbars of the data.

Field	Source	$N_{\text{stars}}/\text{deg}^2$	Events/star/year	Events/deg <sup>2</sup> /year	$\langle t_E \rangle_{300}$	Med( $(t_E)_{300}$ )
Field Avg	S Runs	3.40	15.86±1.9	66.19±15.3	18.7±1.2	13.8±0.9
	M Runs	4.45	14.98±1.8	85.05±20.8	25.4±3.3	15.3±2.1
	Mroz19	6.50	15.66±1.4	100.79±16.1	25.6±1.4	–

poorly by a PSPL model, and 7.0% were multiple events that were fit poorly by a PSPL model. Of the PSPL events that were fit poorly by a PSPL model, some had a strong parallax signal that meant they were fit poorly by the model which did not include parallax. Some, though, had a model that tried to fit some of the random scatter that was added and fit the incorrect model. Overall, most of the multiple events were fit well by a PSPL model and most of the microlensing events that were fit well by a PSPL model are in reality not single.

In addition, we investigated the parameter bias that may be caused by fitting multiple events with PSPL lightcurves. We found that the overall distributions between the input and fit  $t_E$  values (where we use the MAP values for the fit  $t_E$  values) did not change significantly (see Fig. 8). We also investigated the distributions of bias factors (fit value - input value)/fit error. We performed a Kolmogorov-Smirnov two-sample test between the bias distribution for each parameter and a Gaussian distribution. We found that the  $t_E$ ,  $t_0$  and  $b_{sff}$  distributions were consistent with a Gaussian with 99.7% confidence for PSPL, BSPL, PSBL, and BSBL. In both binary and PSPL cases,  $u_0$  and  $m_{base}$  distributions were inconsistent with a Gaussian to with 99.7% confidence. In the case of  $m_{base}$ , this is because the distributions were much narrower than a Gaussian. The  $u_0$  values tended to be larger for the input than the fit values.

For both PSPL and binaries, there was significant bias on an individual event level, especially in  $t_E$  and  $u_0$ . There are gaps and scatter in the data which may affect how these quantities are fit and degeneracies between them which may cause bias. These problems may be addressed by examining the full posteriors in more detail instead of using the MAP quantities. Since the same issues were faced by both PSPL and multiple events, we accept that the estimates we use for  $t_E$ , which are based on system mass, are sufficient for the analysis of the

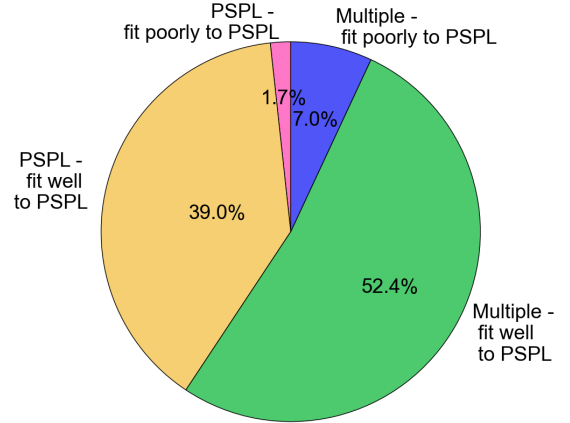


**Figure 7.** Simulated events fit by a PSPL model without parallax which first passed Mock OGLE EWS Cuts (see Section 4) and had significant signal beyond a straight line. 28% of the fit lightcurves had significant signal beyond a straight line, which are those shown in the pie chart. Of the remaining 1,625 events: 39% of events were PSPL events that were fit well by a PSPL model (yellow), 52.4% were multiple event that were fit well by a PSPL model (green), 1.7% were PSPL events that fit poorly by a PSPL model (pink), and 7.0% were multiple events that were fit poorly by a PSPL model (blue). Of the PSPL events that were fit poorly by a PSPL model, some had strong parallax signals which were not captured by our non-parallax model and some had poor fits due to the noise we introduced into the data. The majority of multiple events are fit well by PSPL and the majority of events fit well by PSPL are multiple events masquerading as PSPL.

paper, and will address general bias in microlensing fitting in future work.

#### 5.4. Properties of Binaries Pre- and Post-Microlensing

We investigate how input binary parameters, such as  $\log(a)$  and  $q$ , differ from those post-microlensing, since a difference indicates that a certain kind of system is more likely to lens or

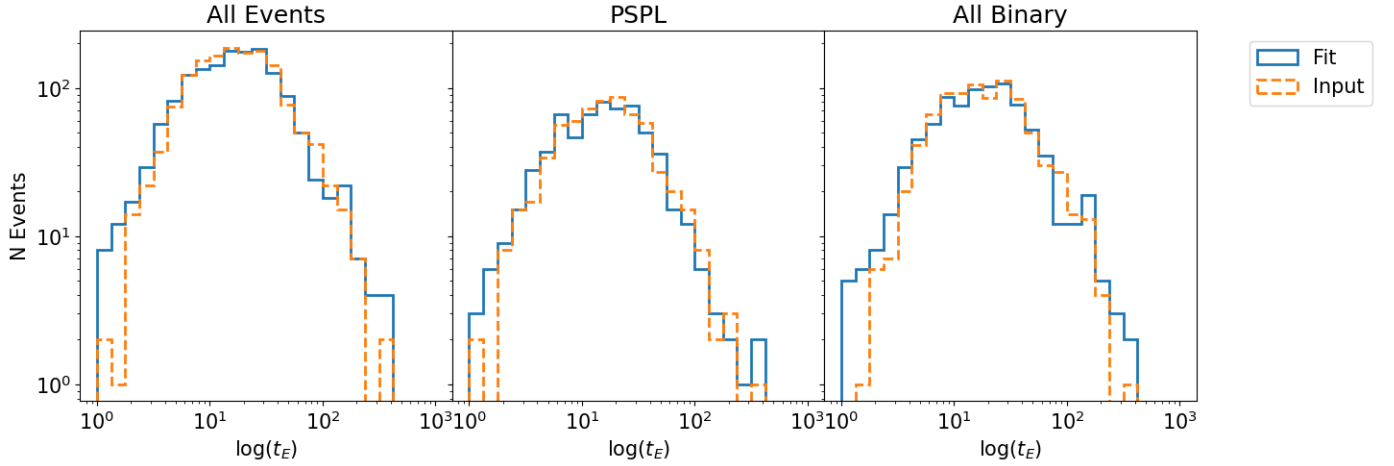


**Figure 8.** Events that were fit by a PSPL model without parallax, which first passed Mock OGLE EWS Cuts (see Section 4). These are events that had a significant signal above a straight line and fit well by a PSPL model. Each panel shows the  $t_E$  distributions of the input parameters (dashed orange) and fit parameters (blue). *Left* is all events, *middle* is all PSPL events, and *right* is all multiple events. On a distribution level, there does not appear to be a significant difference in the input and fit parameters. There is some difference in  $t_E$  at the low  $t_E$  part of the distribution, but we do not explore that in this paper due to the lack of inclusion of brown dwarfs and exoplanets.

be lensed. It also informs how, if we are able to statistically measure binary population parameters via microlensing, we will be biased. Our sample here is with Mock OGLE EWS cuts and includes both single and multi-peaked multiples. As can be seen in the top panel of Fig. 9, we find that binary lenses with a large separation are preferentially not lensed. There seems to be a preferred  $\log(a)$  to be lensed between 1-10 AU. In the bottom panel, we see that multi-peaked binary lenses are even more biased towards  $\log(a)$  values between 1-10 AU, as systems with both small and large separations are less likely to be lensed. In the top panel of Fig. 9, we also see that binary sources are biased towards larger separations. In the bottom panel of Fig. 9, we see that the opposite is true for multi-peaked binary sources which are biased towards smaller  $\log(a)$ . We also observed a drop-off of multi-peaked binary lens events at projected separation  $< 0.3\theta_E$  compared to single peaked binary lens events. In Fig. 10, we see that the  $q$  distributions before microlensing and of the lenses after microlensing are not significantly different. In this case, we are comparing the current mass (as opposed to the ZAMS mass) of the companion/primary, as these are the masses that are observed in the microlensing event.

### 5.5. Multiples Effect on Black Hole Astrometric Follow-Up

In Lam et al. (2020), the limits of  $t_E > 120$  days and  $\pi_E < 0.08$  were established to optimize for selecting black hole targets for astrometric follow-up. As can be seen in Fig. 11, the black holes continue to be isolated in  $\pi_E$ - $t_E$  space. Note that in the M Runs all black holes are in multiple star systems since no binary dynamical evolution is currently included (see Sec. 6.2). The contours of M Run non-black hole events overlaps a small fraction of the gray box, which represents the selection criteria. As can be seen in Fig. 12, the

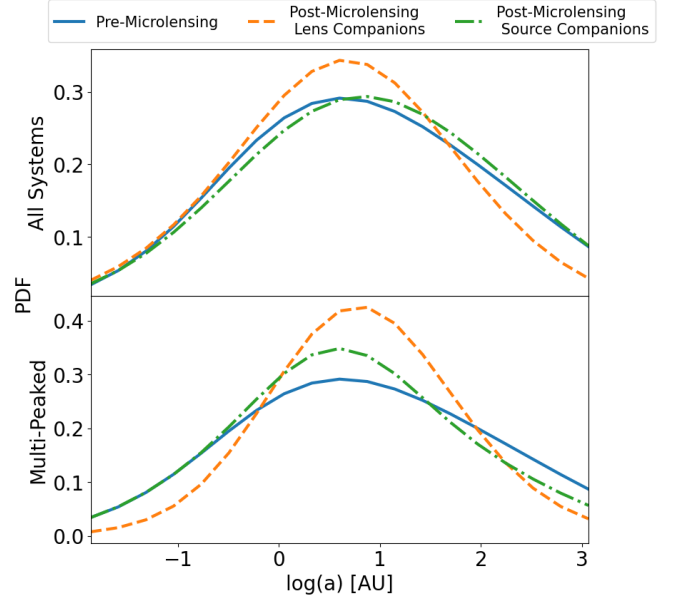


**Figure 9.** We compare the distribution of semi-major axes of binary systems at the population synthesis stage before microlensing (blue), binaries which are lenses (orange dashed), and binaries which are sources (green dash-dotted). The distributions are smoothed with a Gaussian KDE. The top panel has all systems which shows that microlensing tends to disfavor widely separated binary lenses and favor more widely separated binary sources (these results are the same for single peaked events). The lower panel has only multi-peaked systems which shows microlensing tends to disfavor both widely and narrowly separated binary lenses and favor more narrowly separated binary sources in multi-peaked events.

fraction of black holes as a function of  $t_E$  is indistinguishable between M Runs and S Runs. This indicates that multiples

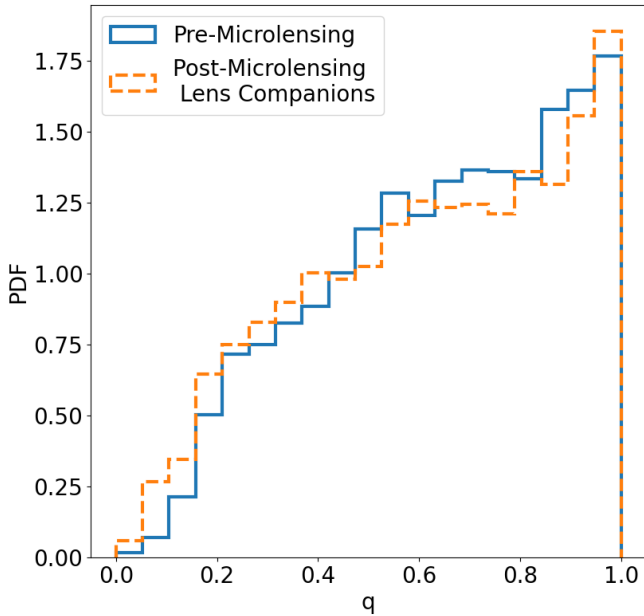


**Figure 10.** We compare the distribution of  $q$  (companion current mass/primary current mass) of binary systems at the population synthesis stage before microlensing (blue) and binaries which are lenses (orange dashed). For any systems where  $q > 1$  due to mass loss such that the primary is the less massive object, we take the inverse of  $q$ . There seems to be no statistically significant change in  $q$  distribution before microlensing and between binary lenses.

will not affect black hole astrometric follow-up candidate selection.

## 6. DISCUSSION

### 6.1. Comparison to Other Simulations

There are a number of other simulations that are used for microlensing population synthesis work. *genulens* (Koshimoto et al. 2021) developed and optimized a parametric model of the Galaxy based on Gaia (Gaia Collaboration et al. 2018), OGLE (Nataf et al. 2013), VVV (Smith et al. 2018), and Brava (Rich et al. 2007; Kunder et al. 2012) star counts, proper motions, and parallaxes, and the OGLE IV  $t_E$  distribution (Mróz et al. 2017, 2019). They included stellar binary lenses that would be undetectable as determined by their caustic size with physical distributions as described by Duchêne & Kraus (2013) and include compact objects following methods in PopSyCLE. They also included exoplanets and brown dwarfs, which PopSyCLE does not currently include. *genulens* is useful as a flexible and parametric galactic model and to assess degenerate solutions to microlensing events using Galactic priors. However, *genulens* has a different purpose than PopSyCLE; it is not designed to generate a set of microlensing events to analyze and, as it uses the OGLE microlensing  $t_E$  distribution as part of its training data, it cannot be used to generate  $t_E$  distributions a priori

and determine how the  $t_E$  distribution changes as the input physics (IMF, IFMR, binary distributions, etc.) change.

GULLS (Penny et al. 2013, 2019)<sup>5</sup> is a microlensing simulation code which is also based on Besançon model of the Milky Way. Following the method of Kerins et al. (2009), GULLS simulates a population of stars and draws source and lens stars from that population, where a magnitude limit is made on the source stars. Those stars are then randomly matched making a microlensing event population. It compares its numbers of stars and event rates to data and finds GULLS natively produces too few microlensing events and stars, so those values are multiplied by a constant factor of 2.33 (Penny et al. 2013) or 2.81 (Penny et al. 2019) to correct for that discrepancy. GULLS has the capability to inject their lightcurves into simulated images for survey planning. They also include exoplanets and brown dwarfs, but do not include compact objects or binaries. As can be seen in Fig. 13 of (Penny et al. 2013), when a  $u_0$  and baseline magnitude observational cut are applied, as is similar to PopSyCLE without binaries, the peak of the  $\log(t_E)$  distribution is  $\log(t_E) < 20$  days.

MaB $\mu$ LS (Awiphan et al. 2016; Specht et al. 2020) is also based on the Besançon model of the Milky Way. Like GULLS, they follow the method of Kerins et al. (2009) by creating catalogs of lenses and sources and finding integrated quantities of optical depth, average  $t_E$ , average  $\mu_{\text{rel}}$ , and event rate. They include brown dwarfs and high-mass free floating planets and the resulting finite source effects. They find the slope of the IMF of brown dwarfs by fitting to OGLE data (Mróz et al. 2019). They also do not include compact objects or binaries. They compare their average quantities as a function of Galactic  $\ell$  and  $b$  to those of OGLE and mostly find agreement with a slight overestimation of  $t_E$  and an underestimation of event rate.

There are a class of simulations that use an analytic model of the Milky Way and make a time-averaged, spatially-averaged mock microlensing survey, pioneered by Han & Gould (1995). In these, one can make predictions for the microlensing  $t_E$  distribution (Niikura et al. 2019) and find how the microlensing parameter distributions change by varying underlying Galactic parameters such as the black hole distribution (Abrams & Takada 2020). In Toki & Takada (2021) they also showed the simulation can be used in a Bayesian study to determine underlying parameters such as mass of the lens from the microlensing lightcurve parameters (PopSyCLE can also be used in this way, see Perkins et al. 2023). Their simulated  $t_E$  distribution can reproduce the  $t_E$  distribution from OGLE data (Niikura et al. 2019). These simulations

<sup>5</sup> In Penny et al. (2013), the code was called MAB $\mu$ LS, but the name was changed to GULLS to distinguish it from the online tool with the same name described in Awiphan et al. (2016).

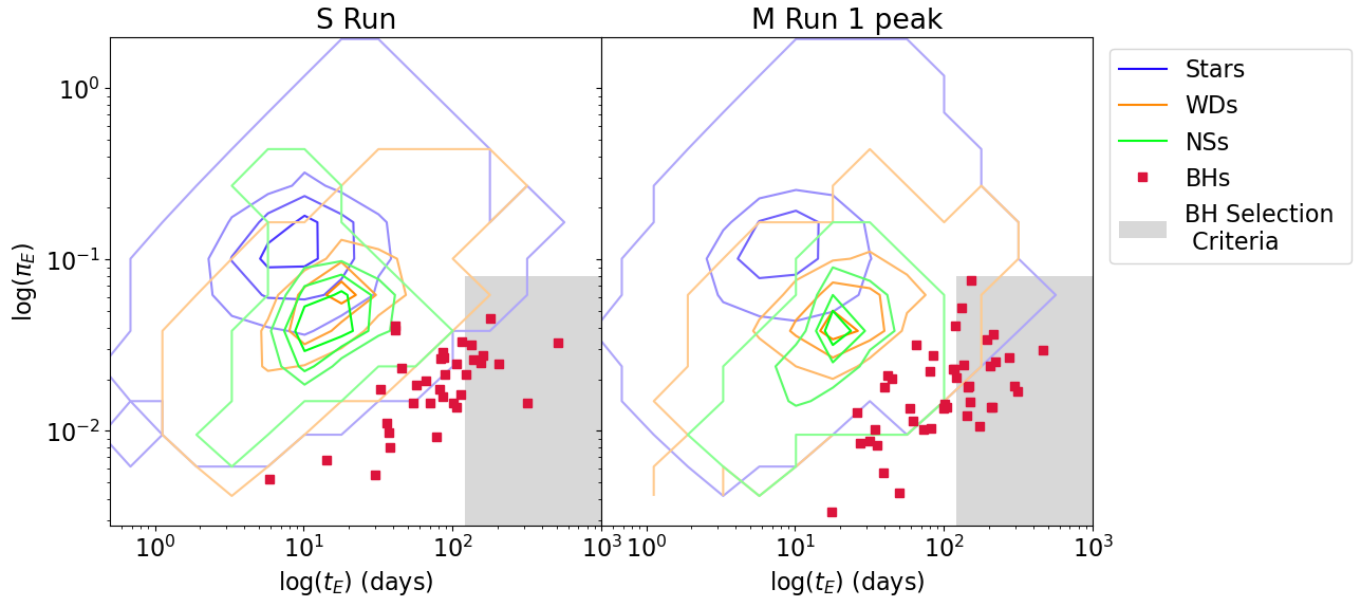


**Figure 11.**  $\pi_E$  vs  $t_E$  for S Runs (left) and single and single-peaked multiples events for M Runs (right). The blue contours are stars, the orange contours are WDs, the green contours are NSs, and the red squares are BHs. The contours are density contours. The grey box is the selection criteria which were established in Lam et al. (2020) of  $t_E > 120$  days and  $\pi_E < 0.08$ . The selection criteria was established to capture the area where black holes are mostly isolated from other events, though the bulk of black hole microlensing events are not in this box. Black holes are still mostly isolated in this box in both the M Runs and the S Runs.

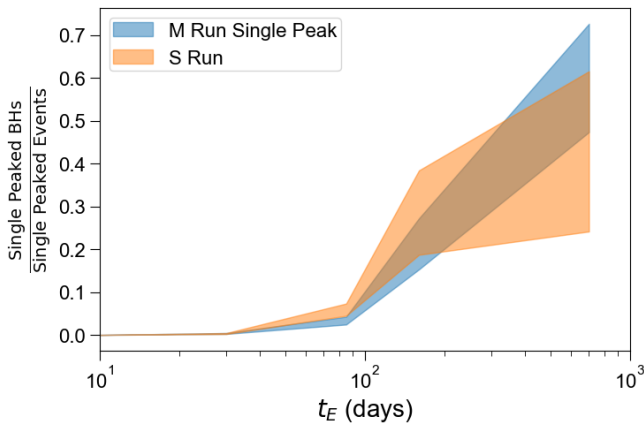


**Figure 12.** Fraction of events which are black holes as a function of the minimum  $t_E$  (Eq. 8) per bin. The contours are  $1\sigma$  Poisson errors. There is no significant difference in the fraction of black holes at any given  $t_E$  between the M Runs and S Runs.

include binaries, but in a rudimentary way – assuming a 40% binary fraction with all equal mass binaries that are close enough to act as a single lens.

Similar analytic approaches are used in other papers including those presenting microlensing survey results (e.g. Sumi et al. 2011; Mróz et al. 2017). These will often do a comparable calculation, but will maximize the likelihood by optimizing the model to best fit their data. Wegg et al. (2017) did so specifically to probe the IMF and binary fraction of the Galactic bulge. They put in a distribution of binary pa-

rameters, and treated those with small separation as acting as one lens and those with large separations as the primary only. Wegg et al. (2017) found they could not distinguish between binary fractions when fitting the OGLE  $t_E$  data. On the other hand, Mróz et al. (2017) found their best model had a 40% binary fraction. In all of these cases, unlike PopSyCLE, they do not simulate individual microlensing events on which we can make observational cuts. They also do not simulate individual objects that have not participated in microlensing which can be used in population statistics work.

## 6.2. Future Work

PopSyCLE’s support for multiplicity, compact objects, and metallicity-dependent IFMRs represents a significant advancement in our ability to simulate microlensing populations. However, there are some limitations and areas we plan to improve in future versions. We currently neglect the orbital motion of binaries, known as xallarap (e.g. Han & Gould 1997; Poindexter et al. 2005), during the mock survey, which can modify the lightcurves and move some events from single-peaked multiples to multi-peaked multiples. Currently we also use a mass and period independent mass ratio distribution and a somewhat simplistic eccentricity distribution which we can improve to include mass and separation dependence in future versions. We also plan to improve the treatment of triple systems.

In this version of PopSyCLE, we use the system mass to determine observable quantities such as  $\pi_E$  and  $t_E$ ; this could lead to a bias in lenses with a massive, distant, and un-



lensed companion. For events with triple systems, when simulating their lightcurves to determine observability, we use whichever primary-companion pair leads to the larger  $\Delta m$ . In reality, triple lens systems should be simulated together to make a single light curve (see Appendix C).

Currently, we evolve our stars as singles rather than including binary interactions, so all of our black holes are in binaries. We plan to incorporate a binary evolution code such as COSMIC (Breivik et al. 2020) or COMPAS (Riley et al. 2022) to model the evolution of systems so that disruption of binaries and other effects can be included. Since the distributions of MF and CSF were drawn from real populations of stars (Lu et al. 2013), it is likely that the stellar distributions are relatively accurate. However, there are certainly effects with compact object formation that are likely not accounted for in these numbers such as mergers or natal kicks which could eject objects (Renzo et al. 2019) and lead to a decreased binary fraction or supernovae which could decrease the masses of the resulting objects (Patton et al. 2022).

As we continue to analyze the affect of binaries on microlensing properties, we will also include additional higher order non-binary effects. In (Golovich et al. 2022), they fit OGLE microlensing events with parallax and Gaussian process, which accounts for systematic noise, and find that the measured  $t_E$  distribution can change from one where the events were fit without these effects. It will be interesting to see how these results are affected by add binarity into the fits.

The addition of multiples to PopSyCLE will also enable many new theoretical studies such as demographic estimates of stars with wide black hole binaries which can allow us to put astrometric binaries found with Gaia (e.g. El-Badry et al. 2023a,b; Chakrabarti et al. 2023) in context; interpreting of surveys searching for black holes via radial velocity (e.g. Clavel et al. 2021); understanding the possibility of white dwarf self lensing (e.g. Nir & Bloom 2023); and quantifying the contamination of exoplanet microlensing with wide binaries (e.g. Han & Gaudi 2008).

## 7. CONCLUSION

We found that multiple system sources and lenses make up the majority of observable microlensing events and thus cannot be neglected. Specifically, we found:

- Over half of microlensing events likely contain a multiple system as a lens or source, many of which can masquerade as single events.
- Adding in multiple systems brings PopSyCLE simulations into agreement with  $t_E$  and event rate data.
- On average, lens binaries are biased away from large semi-major axes and source binaries are biased towards them. Whereas multi-peaked lens binaries are

biased towards average semi-major axes and source binaries are biased towards small semi-major axes.

- Binaries are unlikely to affect black hole candidate selection.

The idea that binaries are important to understanding populations of microlensing events and that they are likely being missed as normal PSPL events is not new. As obvious binary microlensing began to be found, it was conjectured that most microlensing events have binary lenses (Di Stefano 2000) and that many are likely easily misclassified as single lenses (Di Stefano & Perna 1997; Night et al. 2008). It was also thought that binary sources may often be missed by being more easily modeled by a blended single source (Dominik 1998). Griest & Hu (1992) estimated that binary sources would be distinguishable from singles sources a minimum of 2-5% of the time and a maximum of 10-20% of the time. Mao & Paczynski (1991) estimate  $\sim 10\%$  of microlensing events are expected have a “strong” binary signal, but note that binary stars with separations much smaller or larger than their Einstein radius are likely to act like singles. Neglecting multiples could have the impacts outlined here along with potentially leading to overestimates of the optical depth (Di Stefano 2000; Han 2005), but due to the computational challenge of fitting all microlensing events with binary lightcurves, we have yet to systematically do so. As we continue to interpret events from ongoing microlensing surveys and begin to detect microlensing events with new surveys such as the Vera C. Rubin Observatory (Sajadian & Poleski 2019; Abrams & Takada 2020; Abrams et al. 2023) and the Nancy Grace Roman Telescope (Johnson et al. 2020; Lam et al. 2023), it is imperative that we incorporate binaries into our understanding and interpretation of their results.

We thank Guy Nir, Will Dawson, Scott Perkins, and Peter McGill for helpful conversations. This research used resources of the National Energy Research Scientific Computing Center (NERSC), a U.S. Department of Energy Office of Science User Facility located at Lawrence Berkeley National Laboratory, operated under Contract No. DE-AC02-05CH11231 using NERSC award HEP-ERCAP0023758 and HEP-ERCAP0026816. N.S.A., J.R.L., and C. Y. L. acknowledge support from the National Science Foundation under grant No. 1909641 and the Heising-Simons Foundation under grant No. 2022-3542. C. Y. L. acknowledges support from NASA FINESST grant No. 80NSSC21K2043, the H2H8 foundation, and a Carnegie Fellowship and a Harrison Fellowship.

*Software:* Numpy (Harris et al. 2020), Matplotlib (Hunter 2007), Astropy (Astropy Collaboration et al. 2022), pandas (pandas development team 2022; Wes McKinney 2010), SciPy (Virtanen et al. 2020), pymultinest (Buch-

ner et al. 2014), BAGLE, PopSyCLE (Lam et al. 2020), SPISEA (Hosek et al. 2020)

## REFERENCES

- Abbott, B. P., Abbott, R., Abbott, T. D., et al. 2016, *Phys. Rev. Lett.*, 116, 061102, doi: [10.1103/PhysRevLett.116.061102](https://doi.org/10.1103/PhysRevLett.116.061102)
- Abrams, N. S., & Takada, M. 2020, *ApJ*, 905, 121, doi: [10.3847/1538-4357/abc6aa](https://doi.org/10.3847/1538-4357/abc6aa)
- Abrams, N. S., Hundertmark, M. P. G., Khakpash, S., et al. 2023, arXiv e-prints, arXiv:2309.15310, doi: [10.48550/arXiv.2309.15310](https://doi.org/10.48550/arXiv.2309.15310)
- Alcock, C., Allsman, R. A., Alves, D. R., et al. 2000a, *ApJ*, 542, 281, doi: [10.1086/309512](https://doi.org/10.1086/309512)
- Alcock, C., Allsman, R. A., Alves, D., et al. 2000b, *ApJ*, 541, 270, doi: [10.1086/309393](https://doi.org/10.1086/309393)
- Astropy Collaboration, Price-Whelan, A. M., Lim, P. L., et al. 2022, *ApJ*, 935, 167, doi: [10.3847/1538-4357/ac7c74](https://doi.org/10.3847/1538-4357/ac7c74)
- Awiphan, S., Kerins, E., & Robin, A. C. 2016, *MNRAS*, 456, 1666, doi: [10.1093/mnras/stv2625](https://doi.org/10.1093/mnras/stv2625)
- Bennett, D. P., Becker, A. C., Calitz, J. J., et al. 2002, arXiv e-prints, astro. <https://arxiv.org/abs/astro-ph/0207006>
- Bennett, D. P., Bond, I. A., Udalski, A., et al. 2008, *ApJ*, 684, 663, doi: [10.1086/589940](https://doi.org/10.1086/589940)
- Bensby, T., Yee, J. C., Feltzing, S., et al. 2013, *A&A*, 549, A147, doi: [10.1051/0004-6361/201220678](https://doi.org/10.1051/0004-6361/201220678)
- Breivik, K., Coughlin, S., Zevin, M., et al. 2020, *ApJ*, 898, 71, doi: [10.3847/1538-4357/ab9d85](https://doi.org/10.3847/1538-4357/ab9d85)
- Buchner, J., Georgakakis, A., Nandra, K., et al. 2014, *A&A*, 564, A125, doi: [10.1051/0004-6361/201322971](https://doi.org/10.1051/0004-6361/201322971)
- Chakrabarti, S., Simon, J. D., Craig, P. A., et al. 2023, *AJ*, 166, 6, doi: [10.3847/1538-3881/accf21](https://doi.org/10.3847/1538-3881/accf21)
- Clavel, M., Dubus, G., Casares, J., & Babusiaux, C. 2021, *A&A*, 645, A72, doi: [10.1051/0004-6361/202039317](https://doi.org/10.1051/0004-6361/202039317)
- Corral-Santana, J. M., Casares, J., Muñoz-Darias, T., et al. 2016, *A&A*, 587, A61, doi: [10.1051/0004-6361/201527130](https://doi.org/10.1051/0004-6361/201527130)
- Damineli, A., Almeida, L. A., Blum, R. D., et al. 2016, *MNRAS*, 463, 2653, doi: [10.1093/mnras/stw2122](https://doi.org/10.1093/mnras/stw2122)
- Di Stefano, R. 2000, *ApJ*, 541, 587, doi: [10.1086/309474](https://doi.org/10.1086/309474)
- Di Stefano, R., & Perna, R. 1997, *ApJ*, 488, 55, doi: [10.1086/304704](https://doi.org/10.1086/304704)
- Dominik, M. 1998, *A&A*, 333, 893, <https://arxiv.org/abs/astro-ph/9801119>
- Duchêne, G., & Kraus, A. 2013, *ARA&A*, 51, 269, doi: [10.1146/annurev-astro-081710-102602](https://doi.org/10.1146/annurev-astro-081710-102602)
- El-Badry, K., Rix, H.-W., Quataert, E., et al. 2023a, *MNRAS*, 518, 1057, doi: [10.1093/mnras/stac3140](https://doi.org/10.1093/mnras/stac3140)
- El-Badry, K., Rix, H.-W., Cendes, Y., et al. 2023b, *MNRAS*, 521, 4323, doi: [10.1093/mnras/stad799](https://doi.org/10.1093/mnras/stad799)
- Gaia Collaboration, Katz, D., Antoja, T., et al. 2018, *A&A*, 616, A11, doi: [10.1051/0004-6361/201832865](https://doi.org/10.1051/0004-6361/201832865)
- Gaudi, B. S. 2012, *ARA&A*, 50, 411, doi: [10.1146/annurev-astro-081811-125518](https://doi.org/10.1146/annurev-astro-081811-125518)
- Golovich, N., Dawson, W., Bartolić, F., et al. 2022, *ApJS*, 260, 2, doi: [10.3847/1538-4365/ac5969](https://doi.org/10.3847/1538-4365/ac5969)
- Griest, K., & Hu, W. 1992, *ApJ*, 397, 362, doi: [10.1086/171793](https://doi.org/10.1086/171793)
- Griest, K., & Safizadeh, N. 1998, *ApJ*, 500, 37, doi: [10.1086/305729](https://doi.org/10.1086/305729)
- Griest, K., Alcock, C., Axelrod, T. S., et al. 1991, *ApJL*, 372, L79, doi: [10.1086/186028](https://doi.org/10.1086/186028)
- Hamadache, C., Le Guillou, L., Tisserand, P., et al. 2006, *A&A*, 454, 185, doi: [10.1051/0004-6361:20064893](https://doi.org/10.1051/0004-6361:20064893)
- Han, C. 2005, *ApJ*, 633, 410, doi: [10.1086/444614](https://doi.org/10.1086/444614)
- Han, C., & Gaudi, B. S. 2008, *ApJ*, 689, 53, doi: [10.1086/592723](https://doi.org/10.1086/592723)
- Han, C., & Gould, A. 1995, *ApJ*, 449, 521, doi: [10.1086/176076](https://doi.org/10.1086/176076)
- . 1997, *ApJ*, 480, 196, doi: [10.1086/303944](https://doi.org/10.1086/303944)
- Harris, C. R., Millman, K. J., van der Walt, S. J., et al. 2020, *Nature*, 585, 357, doi: [10.1038/s41586-020-2649-2](https://doi.org/10.1038/s41586-020-2649-2)
- Holtzman, J. A., Afonso, C., & Dolphin, A. 2006, *ApJS*, 166, 534, doi: [10.1086/507074](https://doi.org/10.1086/507074)
- Hosek, Matthew W., J., Lu, J. R., Lam, C. Y., et al. 2020, *AJ*, 160, 143, doi: [10.3847/1538-3881/aba533](https://doi.org/10.3847/1538-3881/aba533)
- Hunter, J. D. 2007, *Computing in Science & Engineering*, 9, 90, doi: [10.1109/MCSE.2007.55](https://doi.org/10.1109/MCSE.2007.55)
- Husseiniova, A., McGill, P., Smith, L. C., & Evans, N. W. 2021, *MNRAS*, 506, 2482, doi: [10.1093/mnras/stab1882](https://doi.org/10.1093/mnras/stab1882)
- Hwang, H.-C., Ting, Y.-S., & Zakamska, N. L. 2022, *MNRAS*, 512, 3383, doi: [10.1093/mnras/stac675](https://doi.org/10.1093/mnras/stac675)
- Jaroszynski, M. 2002, *AcA*, 52, 39, doi: [10.48550/arXiv.astro-ph/0203476](https://doi.org/10.48550/arXiv.astro-ph/0203476)
- Jaroszynski, M., Udalski, A., Kubiak, M., et al. 2004, *AcA*, 54, 103. <https://arxiv.org/abs/astro-ph/0408243>
- Jaroszynski, M., Skowron, J., Udalski, A., et al. 2006, *AcA*, 56, 307, doi: [10.48550/arXiv.astro-ph/0701919](https://doi.org/10.48550/arXiv.astro-ph/0701919)
- Jarozński, M., Skowron, J., Udalski, A., et al. 2010, *AcA*, 60, 197, doi: [10.48550/arXiv.1009.5563](https://doi.org/10.48550/arXiv.1009.5563)
- Johnson, S. A., Penny, M., Gaudi, B. S., et al. 2020, *AJ*, 160, 123, doi: [10.3847/1538-3881/aba75b](https://doi.org/10.3847/1538-3881/aba75b)
- Kaczmarek, Z., McGill, P., Evans, N. W., et al. 2023, arXiv e-prints, arXiv:2312.11667, doi: [10.48550/arXiv.2312.11667](https://doi.org/10.48550/arXiv.2312.11667)
- . 2022, *MNRAS*, 514, 4845, doi: [10.1093/mnras/stac1507](https://doi.org/10.1093/mnras/stac1507)
- Kains, N., Calamida, A., Sahu, K. C., et al. 2018, *ApJ*, 867, 37, doi: [10.3847/1538-4357/aae311](https://doi.org/10.3847/1538-4357/aae311)

- Kerins, E., Robin, A. C., & Marshall, D. J. 2009, *MNRAS*, 396, 1202, doi: [10.1111/j.1365-2966.2009.14791.x](https://doi.org/10.1111/j.1365-2966.2009.14791.x)
- Kim, D. J., Kim, H. W., Hwang, K. H., et al. 2018, *AJ*, 155, 76, doi: [10.3847/1538-3881/aaa47b](https://doi.org/10.3847/1538-3881/aaa47b)
- Kiminki, D. C., & Kobulnicky, H. A. 2012, *ApJ*, 751, 4, doi: [10.1088/0004-637X/751/1/4](https://doi.org/10.1088/0004-637X/751/1/4)
- Kiraga, M., & Paczynski, B. 1994, *ApJL*, 430, L101, doi: [10.1086/187448](https://doi.org/10.1086/187448)
- Kobulnicky, H. A., & Fryer, C. L. 2007, *ApJ*, 670, 747, doi: [10.1086/522073](https://doi.org/10.1086/522073)
- Koshimoto, N., Baba, J., & Bennett, D. P. 2021, *ApJ*, 917, 78, doi: [10.3847/1538-4357/ac07a8](https://doi.org/10.3847/1538-4357/ac07a8)
- Kunder, A., Koch, A., Rich, R. M., et al. 2012, *AJ*, 143, 57, doi: [10.1088/0004-6256/143/3/57](https://doi.org/10.1088/0004-6256/143/3/57)
- Lam, C. Y., & Lu, J. R. 2023, arXiv e-prints, arXiv:2308.03302, doi: [10.48550/arXiv.2308.03302](https://doi.org/10.48550/arXiv.2308.03302)
- Lam, C. Y., Lu, J. R., Hosek, Matthew W., J., Dawson, W. A., & Golovich, N. R. 2020, *ApJ*, 889, 31, doi: [10.3847/1538-4357/ab5fd3](https://doi.org/10.3847/1538-4357/ab5fd3)
- Lam, C. Y., Lu, J. R., Udalski, A., et al. 2022, *ApJL*, 933, L23, doi: [10.3847/2041-8213/ac7442](https://doi.org/10.3847/2041-8213/ac7442)
- Lam, C. Y., Abrams, N., Andrews, J., et al. 2023, arXiv e-prints, arXiv:2306.12514, doi: [10.48550/arXiv.2306.12514](https://doi.org/10.48550/arXiv.2306.12514)
- Lu, J. R., Do, T., Ghez, A. M., et al. 2013, *ApJ*, 764, 155, doi: [10.1088/0004-637X/764/2/155](https://doi.org/10.1088/0004-637X/764/2/155)
- Lu, J. R., Ghez, A. M., Hornstein, S. D., et al. 2009, *ApJ*, 690, 1463, doi: [10.1088/0004-637X/690/2/1463](https://doi.org/10.1088/0004-637X/690/2/1463)
- Lu, J. R., Sinukoff, E., Ofek, E. O., Udalski, A., & Kozłowski, S. 2016, *ApJ*, 830, 41, doi: [10.3847/0004-637X/830/1/41](https://doi.org/10.3847/0004-637X/830/1/41)
- Mao, S., & Paczynski, B. 1991, *ApJL*, 374, L37, doi: [10.1086/186066](https://doi.org/10.1086/186066)
- Mao, S., Smith, M. C., Woźniak, P., et al. 2002, *MNRAS*, 329, 349, doi: [10.1046/j.1365-8711.2002.04986.x](https://doi.org/10.1046/j.1365-8711.2002.04986.x)
- Medford, M. S., Abrams, N. S., Lu, J. R., Nugent, P., & Lam, C. Y. 2023, *ApJ*, 947, 24, doi: [10.3847/1538-4357/acba8f](https://doi.org/10.3847/1538-4357/acba8f)
- Moe, M., & Di Stefano, R. 2017, *ApJS*, 230, 15, doi: [10.3847/1538-4365/aa6fb6](https://doi.org/10.3847/1538-4365/aa6fb6)
- Moe, M., & Kratter, K. M. 2021, *MNRAS*, 507, 3593, doi: [10.1093/mnras/stab2328](https://doi.org/10.1093/mnras/stab2328)
- Moniez, M., Sajadian, S., Karami, M., Rahvar, S., & Ansari, R. 2017, *A&A*, 604, A124, doi: [10.1051/0004-6361/201730488](https://doi.org/10.1051/0004-6361/201730488)
- Mróz, P., Udalski, A., & Gould, A. 2022, *ApJL*, 937, L24, doi: [10.3847/2041-8213/ac90bb](https://doi.org/10.3847/2041-8213/ac90bb)
- Mróz, P., Udalski, A., Skowron, J., et al. 2017, *Nature*, 548, 183, doi: [10.1038/nature23276](https://doi.org/10.1038/nature23276)
- . 2019, *ApJS*, 244, 29, doi: [10.3847/1538-4365/ab426b](https://doi.org/10.3847/1538-4365/ab426b)
- Nataf, D. M., Gould, A., Fouqué, P., et al. 2013, *ApJ*, 769, 88, doi: [10.1088/0004-637X/769/2/88](https://doi.org/10.1088/0004-637X/769/2/88)
- Navarro, M. G., Contreras Ramos, R., Minniti, D., et al. 2020, *ApJ*, 893, 65, doi: [10.3847/1538-4357/ab7a9d](https://doi.org/10.3847/1538-4357/ab7a9d)
- Night, C., Di Stefano, R., & Schwamb, M. 2008, *ApJ*, 686, 785, doi: [10.1086/590320](https://doi.org/10.1086/590320)
- Niikura, H., Takada, M., Yokoyama, S., Sumi, T., & Masaki, S. 2019, *PhRvD*, 99, 083503, doi: [10.1103/PhysRevD.99.083503](https://doi.org/10.1103/PhysRevD.99.083503)
- Nir, G., & Bloom, J. S. 2023, arXiv e-prints, arXiv:2311.14392, doi: [10.48550/arXiv.2311.14392](https://doi.org/10.48550/arXiv.2311.14392)
- Paczynski, B. 1986, *ApJ*, 304, 1, doi: [10.1086/164140](https://doi.org/10.1086/164140)
- pandas development team, T. 2022, pandas-dev/pandas: Pandas, v1.5.2, Zenodo, doi: [10.5281/zenodo.7344967](https://doi.org/10.5281/zenodo.7344967)
- Park, H., Udalski, A., Han, C., et al. 2013, *ApJ*, 778, 134, doi: [10.1088/0004-637X/778/2/134](https://doi.org/10.1088/0004-637X/778/2/134)
- Patton, R. A., Sukhbold, T., & Eldridge, J. J. 2022, *MNRAS*, 511, 903, doi: [10.1093/mnras/stab3797](https://doi.org/10.1093/mnras/stab3797)
- Penny, M. T., Gaudi, B. S., Kerins, E., et al. 2019, *ApJS*, 241, 3, doi: [10.3847/1538-4365/aaf6b9](https://doi.org/10.3847/1538-4365/aaf6b9)
- Penny, M. T., Kerins, E., Rattenbury, N., et al. 2013, *MNRAS*, 434, 2, doi: [10.1093/mnras/stt927](https://doi.org/10.1093/mnras/stt927)
- Perkins, S. E., McGill, P., Dawson, W., et al. 2023, arXiv e-prints, arXiv:2310.03943, doi: [10.48550/arXiv.2310.03943](https://doi.org/10.48550/arXiv.2310.03943)
- Poindexter, S., Afonso, C., Bennett, D. P., et al. 2005, *ApJ*, 633, 914, doi: [10.1086/468182](https://doi.org/10.1086/468182)
- Rasskazov, A., Fragione, G., Leigh, N. W. C., et al. 2019, *ApJ*, 878, 17, doi: [10.3847/1538-4357/ab1c5d](https://doi.org/10.3847/1538-4357/ab1c5d)
- Renzo, M., Zapartas, E., de Mink, S. E., et al. 2019, *A&A*, 624, A66, doi: [10.1051/0004-6361/201833297](https://doi.org/10.1051/0004-6361/201833297)
- Rich, R. M. 2013, in *Planets, Stars and Stellar Systems. Volume 5: Galactic Structure and Stellar Populations*, ed. T. D. Oswalt & G. Gilmore, Vol. 5, 271, doi: [10.1007/978-94-007-5612-0\\_6](https://doi.org/10.1007/978-94-007-5612-0_6)
- Rich, R. M., Reitzel, D. B., Howard, C. D., & Zhao, H. 2007, *ApJL*, 658, L29, doi: [10.1086/513509](https://doi.org/10.1086/513509)
- Riley, J., Agrawal, P., Barrett, J. W., et al. 2022, *ApJS*, 258, 34, doi: [10.3847/1538-4365/ac416c](https://doi.org/10.3847/1538-4365/ac416c)
- Robin, A. C., Reylé, C., Derrière, S., & Picaud, S. 2003, *A&A*, 409, 523, doi: [10.1051/0004-6361:20031117](https://doi.org/10.1051/0004-6361:20031117)
- Rodriguez, A. C., Mróz, P., Kulkarni, S. R., et al. 2022, *ApJ*, 927, 150, doi: [10.3847/1538-4357/ac51cc](https://doi.org/10.3847/1538-4357/ac51cc)
- Rose, S., Lam, C. Y., Lu, J. R., et al. 2022, *ApJ*, 941, 116, doi: [10.3847/1538-4357/aca09d](https://doi.org/10.3847/1538-4357/aca09d)
- Sahu, K. C., Anderson, J., Casertano, S., et al. 2022, *ApJ*, 933, 83, doi: [10.3847/1538-4357/ac739e](https://doi.org/10.3847/1538-4357/ac739e)
- Sajadian, S., & Poleski, R. 2019, *ApJ*, 871, 205, doi: [10.3847/1538-4357/aafa1d](https://doi.org/10.3847/1538-4357/aafa1d)
- Schlegel, D. J., Finkbeiner, D. P., & Davis, M. 1998, *ApJ*, 500, 525, doi: [10.1086/305772](https://doi.org/10.1086/305772)
- Sharma, S., Bland-Hawthorn, J., Johnston, K. V., & Binney, J. 2011, *ApJ*, 730, 3, doi: [10.1088/0004-637X/730/1/3](https://doi.org/10.1088/0004-637X/730/1/3)
- Skowron, J., Jaroszynski, M., Udalski, A., et al. 2007, *AcA*, 57, 281, doi: [10.48550/arXiv.0802.3704](https://doi.org/10.48550/arXiv.0802.3704)
- Skowron, J., Udalski, A., Kozłowski, S., et al. 2016, *AcA*, 66, 1, <https://arxiv.org/abs/1604.01966>

- Smith, L. C., Lucas, P. W., Kurtev, R., et al. 2018, *MNRAS*, 474, 1826, doi: [10.1093/mnras/stx2789](https://doi.org/10.1093/mnras/stx2789)
- Smith, M. C., Woźniak, P., Mao, S., & Sumi, T. 2007, *MNRAS*, 380, 805, doi: [10.1111/j.1365-2966.2007.12130.x](https://doi.org/10.1111/j.1365-2966.2007.12130.x)
- Specht, D., Kerins, E., Awiphan, S., & Robin, A. C. 2020, *MNRAS*, 498, 2196, doi: [10.1093/mnras/staa2375](https://doi.org/10.1093/mnras/staa2375)
- Street, R. A., Choi, J. Y., Tsapras, Y., et al. 2013, *ApJ*, 763, 67, doi: [10.1088/0004-637X/763/1/67](https://doi.org/10.1088/0004-637X/763/1/67)
- Sukhbold, T., Ertl, T., Woosley, S. E., Brown, J. M., & Janka, H. T. 2016, *ApJ*, 821, 38, doi: [10.3847/0004-637X/821/1/38](https://doi.org/10.3847/0004-637X/821/1/38)
- Sukhbold, T., & Woosley, S. E. 2014, *ApJ*, 783, 10, doi: [10.1088/0004-637X/783/1/10](https://doi.org/10.1088/0004-637X/783/1/10)
- Sumi, T., Abe, F., Bond, I. A., et al. 2003, *ApJ*, 591, 204, doi: [10.1086/375212](https://doi.org/10.1086/375212)
- Sumi, T., Woźniak, P. R., Udalski, A., et al. 2006, *ApJ*, 636, 240, doi: [10.1086/497951](https://doi.org/10.1086/497951)
- Sumi, T., Kamiya, K., Bennett, D. P., et al. 2011, *Nature*, 473, 349, doi: [10.1038/nature10092](https://doi.org/10.1038/nature10092)
- Sumi, T., Bennett, D. P., Bond, I. A., et al. 2013, *ApJ*, 778, 150, doi: [10.1088/0004-637X/778/2/150](https://doi.org/10.1088/0004-637X/778/2/150)
- Tisserand, P., Le Guillou, L., Afonso, C., et al. 2007, *A&A*, 469, 387, doi: [10.1051/0004-6361/20066017](https://doi.org/10.1051/0004-6361/20066017)
- Toki, S., & Takada, M. 2021, arXiv e-prints, arXiv:2103.13015, doi: [10.48550/arXiv.2103.13015](https://doi.org/10.48550/arXiv.2103.13015)
- Tokovinin, A. 2020, *MNRAS*, 496, 987, doi: [10.1093/mnras/staa1639](https://doi.org/10.1093/mnras/staa1639)
- Udalski, A., Szymański, M. K., & Szymański, G. 2015, *AcA*, 65, 1, doi: [10.48550/arXiv.1504.05966](https://doi.org/10.48550/arXiv.1504.05966)
- Van De Kamp, P. 1967, *Principles of astrometry*
- Virtanen, P., Gommers, R., Oliphant, T. E., et al. 2020, *Nature Methods*, 17, 261, doi: [10.1038/s41592-019-0686-2](https://doi.org/10.1038/s41592-019-0686-2)
- Wegg, C., Gerhard, O., & Portail, M. 2017, *ApJL*, 843, L5, doi: [10.3847/2041-8213/aa794e](https://doi.org/10.3847/2041-8213/aa794e)
- Wes McKinney. 2010, in *Proceedings of the 9th Python in Science Conference*, ed. Stéfan van der Walt & Jarrod Millman, 56 – 61, doi: [10.25080/Majora-92bf1922-00a](https://doi.org/10.25080/Majora-92bf1922-00a)
- Wiktorowicz, G., Wyrzykowski, Ł., Chruslinska, M., et al. 2019, *ApJ*, 885, 1, doi: [10.3847/1538-4357/ab45e6](https://doi.org/10.3847/1538-4357/ab45e6)
- Wyrzykowski, Ł., & Mandel, I. 2020, *A&A*, 636, A20, doi: [10.1051/0004-6361/201935842](https://doi.org/10.1051/0004-6361/201935842)
- Wyrzykowski, Ł., Rybicki, K. A., Kruszyńska, K., et al. 2019, in *Southern Horizons in Time-Domain Astronomy*, ed. R. E. Griffin, Vol. 339, 16–19, doi: [10.1017/S1743921318002107](https://doi.org/10.1017/S1743921318002107)
- Wyrzykowski, Ł., Kruszyńska, K., Rybicki, K. A., et al. 2023, *A&A*, 674, A23, doi: [10.1051/0004-6361/202243756](https://doi.org/10.1051/0004-6361/202243756)
- Zhai, R., Rodriguez, A. C., Lam, C. Y., et al. 2023, arXiv e-prints, arXiv:2311.18627, doi: [10.48550/arXiv.2311.18627](https://doi.org/10.48550/arXiv.2311.18627)
- Zhao, H. 1996, *MNRAS*, 283, 149, doi: [10.1093/mnras/283.1.149](https://doi.org/10.1093/mnras/283.1.149)

## APPENDIX

## A. FIELD PARAMETERS

In Table 8, one can find the field-by-field comparison of S Runs, M Runs, and Mróz et al. (2019).

**Table 8.** This table compares the individual field results for singles-only simulations (S Runs) and single-peaked multiples+singles simulations (M Runs) to Mróz et al. (2019) values by making the cuts indicated in Table 3. We compare the number of stars/deg<sup>2</sup> (where multiple star systems are counted a single blended star), events/star/year, events/deg<sup>2</sup>/year and the mean  $t_E$  between 0.5 and 300 days. We also compute the median  $t_E$  between 0.5 and 300 days.  $N_{\text{stars}}$  is  $10^{-6}$  the value in the simulation. The average between these fields can be found in Table 7.

Field	Source	$N_{\text{stars}}/\text{deg}^2$	Events/star/year	Events/deg <sup>2</sup> /year	$\langle t_E \rangle_{300}$	Med( $(t_E)_{300}$ )
BLG500	S Runs	3.37	26.14±2.9	88.09±9.7	21.2±2.0	15.5±2.0
	M Runs	4.35	21.24±2.3	92.39±10.0	20.3±2.4	10.5±2.4
	Mroz19	4.84	23.90±2.0	168.80±13.7	18.8±1.6	–
BLG501	S Runs	8.75	32.05±2.0	280.38±17.4	18.4±1.4	12.2±1.4
	M Runs	11.43	32.52±1.7	371.70±20.0	21.1±1.5	12.1±1.5
	Mroz19	9.51	24.10±1.4	222.90±12.9	20.5±1.1	–
BLG504	S Runs	3.11	17.61±2.5	54.79±7.7	17.5±2.6	12.8±2.6
	M Runs	4.07	18.48±2.2	75.20±9.0	23.1±2.6	16.5±2.6
	Mroz19	8.47	16.90±1.2	134.30±9.1	20.0±1.2	–
BLG505	S Runs	7.06	20.99±1.8	148.25±12.6	17.0±1.4	13.1±1.4
	M Runs	9.29	24.29±1.7	225.60±15.6	18.5±1.3	12.5±1.3
	Mroz19	13.59	22.20±1.1	265.30±12.8	21.8±1.5	–
BLG506	S Runs	3.83	21.33±2.4	81.64±9.4	18.9±2.1	12.4±2.1
	M Runs	5.14	21.93±2.1	112.80±11.0	14.8±1.3	11.0±1.3
	Mroz19	9.18	16.50±1.1	137.40±8.9	28.0±2.9	–
BLG507	S Runs	3.77	12.54±1.9	47.27±7.1	14.9±1.8	10.3±1.8
	M Runs	5.02	13.28±1.7	66.60±8.5	21.8±3.3	14.4±3.3
	Mroz19	8.01	12.30±0.9	87.30±6.1	22.9±1.4	–
BLG511	S Runs	3.64	15.04±2.1	54.79±7.7	20.7±2.5	17.2±2.5
	M Runs	4.75	13.12±1.7	62.31±8.2	22.9±3.0	14.4±3.0
	Mroz19	9.61	13.50±1.0	113.90±8.1	24.5±2.0	–
BLG512	S Runs	5.96	17.50±1.8	104.20±10.6	16.5±1.6	10.5±1.6
	M Runs	7.79	17.24±1.5	134.28±12.0	21.0±1.9	14.5±1.9
	Mroz19	12.49	14.00±0.9	148.50±9.0	24.0±1.5	–
BLG527	S Runs	2.04	2.63±1.2	5.37±2.4	12.1±1.5	11.8±1.5
	M Runs	2.44	2.64±1.1	6.45±2.6	43.6±10.4	41.5±10.4
	Mroz19	4.54	5.50±0.9	21.90±3.5	39.5±5.0	–
BLG534	S Runs	3.26	20.77±2.6	67.68±8.5	17.2±2.3	11.2±2.3
	M Runs	4.28	16.30±2.0	69.83±8.7	16.2±1.9	10.2±1.9

**Table 8** continued

**Table 8** (*continued*)

Field	Source	$N_{\text{stars}}/\text{deg}^2$	Events/star/year	Events/deg <sup>2</sup> /year	$\langle t_E \rangle_{300}$	Med( $(t_E)_{300}$ )
BLG535	Mroz19	6.47	17.20±1.3	104.80±8.1	20.8±1.6	–
	S Runs	2.57	10.46±2.1	26.86±5.4	14.7±2.4	9.8±2.4
	M Runs	3.39	14.88±2.2	50.49±7.4	27.6±4.8	13.2±4.8
BLG611	Mroz19	5.41	15.20±1.1	85.20±6.4	25.7±1.7	–
	S Runs	3.66	18.76±2.3	68.75±8.6	17.9±2.1	13.9±2.1
	M Runs	4.95	17.13±1.9	84.87±9.5	23.2±3.8	12.4±3.8
BLG629	Mroz19	4.95	16.20±1.3	70.00±5.7	21.8±1.6	–
	S Runs	1.49	1.44±1.0	2.15±1.5	22.4±3.0	22.4±3.0
	M Runs	1.78	1.81±1.0	3.22±1.9	49.4±34.4	11.1±34.4
BLG645	Mroz19	3.26	3.40±1.1	9.70±3.1	36.7±7.8	–
	S Runs	0.47	2.26±2.3	1.07±1.1	11.3±0.0	11.3±0.0
	M Runs	0.57	5.63±3.2	3.22±1.9	69.3±35.5	37.5±35.5
BLG646	Mroz19	2.38	13.60±1.9	29.20±4.0	34.3±4.5	–
	S Runs	0.44	12.12±5.4	5.37±2.4	34.5±17.5	22.3±17.5
	M Runs	0.55	5.91±3.4	3.22±1.9	11.4±3.8	8.3±3.8
BLG648	Mroz19	3.64	8.30±1.2	26.30±3.7	31.7±4.1	–
	S Runs	1.24	10.36±3.0	12.89±3.7	25.5±6.2	18.3±6.2
	M Runs	1.53	9.11±2.5	13.97±3.9	19.8±5.0	13.0±5.0
BLG652	Mroz19	2.04	18.30±2.4	33.20±4.4	24.0±2.8	–
	S Runs	2.59	21.97±3.0	56.94±7.8	21.0±2.4	14.0±2.4
	M Runs	3.47	13.92±2.1	48.34±7.2	17.0±2.8	12.6±2.8
BLG675	Mroz19	4.68	14.20±1.6	60.00±6.9	24.9±2.6	–
	S Runs	3.94	21.54±2.4	84.87±9.5	14.2±1.5	10.2±1.5
	M Runs	5.24	20.30±2.0	106.35±10.7	17.1±1.8	10.2±1.8
	Mroz19	4.03	26.50±2.3	95.50±8.3	21.0±1.8	–

## B. MICROLENSING MODEL DEFINITIONS

In this section, we make the definitions of microlensing configurations explicit. See Table 10 for the standard names and descriptions of these models. We also include how we define  $t_E$  in each of these cases and the number of lightcurves simulated in Section 2.2.5.

In the cases of PSBL, BSPL, and BSBL, we simulate a single lightcurve for the event. However, for triples, we simulate multiple lightcurves and use the one with the largest  $\Delta m$ . The following are the examples of systems we simulate:

- Triple lens and binary source:
  - Primary lens + companion lens 1 + primary source + companion source
  - Primary lens + companion lens 2 + primary source + companion source
- Triple lens and triple source:
  - Primary lens + companion lens 1 + primary source + companion source 1
  - Primary lens + companion lens 1 + primary source + companion source 2
  - Primary lens + companion lens 2 + primary source + companion source 1

**Table 9.** Model definitions

Name	Abbreviation	Description	$t_E$	# lightcurves sim
Point-Source Point-Lens	PSPL	One Source and One Lens	$t_E \propto \sqrt{M_L}$	1
Point-Source Binary-Lens	PSBL	One Source and Two Lenses	$t_E \propto \sqrt{M_{L1} + M_{L2}}$	1
Binary-Source Point-Lens	BSPL	Two Sources and One Lens	$t_E \propto \sqrt{M_L}$	1
Binary-Source Binary-Lens	BSBL	Two Sources and Two Lenses	$t_E \propto \sqrt{M_{L1} + M_{L2}}$	1
Point-Source Triple-Lens	PSTL	One Source and Three Lenses	$t_E \propto \sqrt{M_{L1} + M_{L2} + M_{L3}}$	2
Triple-Source Point-Lens	TSPL	Three Sources and One Lens	$t_E \propto \sqrt{M_L}$	2
Binary-Source Triple-Lens	BSTL	Two Sources and Three Lenses	$t_E \propto \sqrt{M_{L1} + M_{L2} + M_{L3}}$	2
Triple-Source Binary-Lens	TSBL	Three Sources and Two Lenses	$t_E \propto \sqrt{M_{L1} + M_{L2}}$	2
Triple-Source Triple-Lens	TSTL	Three Sources and Three Lenses	$t_E \propto \sqrt{M_{L1} + M_{L2} + M_{L3}}$	4

NOTE—These are summaries of the definitions of microlensing configurations included in this paper.  $t_E$  is defined as Eq. 8 where the  $M$  value in  $\theta_E$  (Eq. 7) is the square root of the total system mass of the lens. The number of lightcurves simulated refers to Section 2.2.5 where, since we only have binary models, we simulate multiple lightcurves for triple systems and select the one with the highest  $\Delta m$ . See the body of Appendix B for examples.

– Primary lens + companion lens 2 + primary source + companion source 2

The parameters for all these lightcurves are stored in the `lightcurves.fits` table where each bullet point would be an entry in that file. We then choose the lightcurve with the largest  $\Delta m$  as the microlensing event. Whether it was used or not is indicated in the lightcurves table.

C. TRIPLES

10.4% of all events and 10.1% of single peaked events have a triple lens or source (see Table 10 for a further breakdown). Since we did not simulate triple lens or source lightcurves and instead used the method as described in Appendix B, we will verify that there is a significant difference between M Runs and S Runs regardless of the inclusion of triples.

More massive objects are more likely to have a higher number of and more massive companions ( $q$  is not dependent on mass, but the same  $q$  corresponds to a more massive companion for a massive primary). So, even if we had limited these objects to one companion, they would likely still make up long  $t_E$  events.

We can integrate the total number of single-peaked events with  $t_E > 30$  days with and without triples. Roughly 50% of the difference between M Runs and S Runs is contributed by triples. However, this represents the most extreme conclusion where correctly treated triples would yield multi-peaked or unobservable events instead of single-peaked events. This is unlikely to be the case, in particular, for triple sources, which make up roughly half of all triple systems. We conclude that regardless of our treatment of triples, M Runs are a better physical model for the observed  $t_E$  distribution.

**Table 10.** Triple breakdown

Model	Percentage of all events
PSTL	2.7%
TSPL	4.9%
BSTL	1.6%
TSBL	0.9%
TSTL	0.2%

NOTE—10.4% of all simulated events have a triple lens or source. This is a breakdown of whether they are triple lenses, sources, or both.